

FH Aachen  
*University of Applied Sciences*  
Fachbereich 6 Luft- und Raumfahrttechnik  
*Department of Aerospace Engineering*  
Luft- und Raumfahrttechnik (B.Eng.)  
*Aerospace Engineering (B.Eng.)*

# **Ultrasonic anemometry for the spatial distributed measurement of rotor wakes**

Bachelor thesis for the degree of  
**Bachelor of Engineering (B.Eng.)**

presented by  
Till Silas Weise  
Matr.Nr.:3279423

16.07.2024

First examiner:  
Second examiner:

Prof. Dr.-Ing. Philipp Hartmann  
Dr.-Ing. Johannes Braukmann

## **Erklärung**

Ich versichere hiermit, dass ich die vorliegende Arbeit selbständig verfasst und keine anderen als die im Quellenverzeichnis angegebenen Quellen benutzt habe. Stellen, die wörtlich oder sinngemäß aus veröffentlichten oder noch nicht veröffentlichten Quellen entnommen sind, sind als solche kenntlich gemacht. Die Zeichnungen oder Abbildungen in dieser Arbeit sind von mir selbst erstellt worden oder mit einem entsprechenden Quellennachweis versehen. Diese Arbeit ist in gleicher oder ähnlicher Form noch bei keiner anderen Prüfungsbehörde eingereicht worden.

Göttingen den 16.07.2024,

(Till Silas Weise)



## Abstract

The Institute of Aerodynamics and Flow Technology of the German Aerospace Center (DLR), in Göttingen is investigating the outwash of single and multirotor aircraft hovering in ground effect. Due to the complex nature of the outwash, especially in the case of multirotor aircraft, a spacial distributed measuring system is needed to investigate the outwash. A suitable measurement technique is an array of ultrasonic anemometers, due to their low complexity and ability to measure even low velocities accurately. Commercially available sensors are costly and do not feature a method for synchronization. Another challenge is the size requirement of under 100 mm × 100 mm × 100 mm.

A 2D ultrasonic anemometer with the required features is developed. The sensor is tested in a wind tunnel campaign and calibrated. The occurring measurement errors are examined and if possible corrected. It has been found that building a small scale ultrasonic anemometer is viable but that some errors occur due to the reduced size of the sensor.

## Kurzfassung

Das Institut für Aerodynamik und Strömungstechnik des Deutschen Zentrums für Luft- und Raumfahrt (DLR) in Göttingen untersucht den Bodenstrahl von schwebenden Ein- und Mehrrotor-Senkrechtstartern. Aufgrund der Komplexität der im Bodenstrahl auftretenden Geschwindigkeitsfeldern, insbesondere bei mehrrotorigen Senkrechtstartern, ist für die Untersuchung ein räumlich verteiltes Messsystem erforderlich. Eine geeignete Messtechnik ist die verteilte Messung mit Ultraschallanemometern, die sich insbesondere durch geringe Komplexität und hohe Genauigkeit auch bei niedrigen Geschwindigkeiten auszeichnet. Kommerziell erhältliche Sensoren sind teuer und verfügen über keine Synchronisationsmöglichkeit. Eine weitere Herausforderung ist die erforderliche Größe von weniger als 100 mm × 100 mm × 100 mm.

In dieser Arbeit wird ein 2D-Ultraschallanemometer mit den erforderlichen Eigenschaften entwickelt. Anschließend wird der Sensor im Windkanal getestet und kalibriert. Auftretende Messfehler werden untersucht und wenn möglich korrigiert. Es hat sich gezeigt, dass der Bau eines Ultraschallanemometers in kleinem Maßstab machbar ist, dass aber aufgrund der geringen Größe des Sensors einige Messfehler auftreten.

## Table of Contents

|   |           |
|---|-----------|
| <b>Table of Contents</b>  | <b>V</b>  |
| <b>1 Introduction</b>   | <b>1</b>  |
| <b>2 Theoretical Background</b>                                 | <b>3</b>  |
| 2.1 Measurement Principle . . . . .                             | 3         |
| 2.2 Transducer Shadow . . . . .                                 | 6         |
| 2.3 Cross-Correlation . . . . .                                 | 6         |
| 2.4 Phase Shift Keying . . . . .                                | 7         |
| 2.5 Cross Flow Correction . . . . .                             | 7         |
| <b>3 Implementation</b>   | <b>9</b>  |
| 3.1 Hardware . . . . .  | 9         |
| 3.2 Software . . . . .  | 12        |
| 3.2.1 Data Acquisition . . . . .                                | 12        |
| Sending and Receiving . . . . .                                 | 12        |
| Key Pattern . . . . .   | 13        |
| 3.2.2 Data Processing . . . . .                                 | 14        |
| Filtering . . . . .   | 14        |
| 1D Measurement . . . . .  | 15        |
| 2D Measurement . . . . .  | 17        |
| 3.2.3 Triggering . . . . .                                      | 18        |
| <b>4 Calibration, Correction, and Validation</b>                | <b>19</b> |
| 4.1 Experimental Setup . . . . .                                | 19        |
| 4.2 Calibration of Velocity Offset and Magnitude . . . . .      | 19        |
| 4.3 Correction for Elongation of the Measurement Path . . . . . | 21        |
| 4.4 Statistical Error . . . . .                                 | 22        |
| 4.5 Velocity Correction . . . . .                               | 27        |
| Uncorrected Velocities . . . . .                                | 29        |
| Kaimal-Gaynor Correction . . . . .                              | 30        |
| Map Correction . . . . .  | 31        |
| Matrix Correction . . . . .                                     | 33        |
| Comparison . . . . .  | 35        |

|                                 |           |
|---------------------------------|-----------|
| <b>5 Conclusion and Outlook</b> | <b>40</b> |
| <b>List of Symbols</b>          | <b>42</b> |
| <b>Literature</b>               | <b>45</b> |

## 1 Introduction

In order to reduce travel time and gain higher flexibility, solutions such as urban air taxis are being evaluated. These air taxis are typically designed to take off vertically, in a manner similar to helicopters. Unlike helicopters, many urban air taxi concepts make use of multirotor setups. For an aircraft to achieve vertical flight, an amount of thrust equal to the weight force acting upon itself, is needed. In order to generate thrust, a certain volume of air must be accelerated vertically, which in turn creates a downwash.

In the presence of the ground or other sufficiently large obstacles below the rotor plane, the downwash is redirected by the ground or the obstacle. This redirected flow is also called outwash, and is approximately parallel to the surface of the object and is thus forced into an approximately 2D flow plane. This phenomenon is called the ground effect. The ground effect can lead to very high local flow velocities.

The outwash of Helicopter is approximately azimuth symmetrical. Unlike helicopters, many urban air taxi concepts make use of multiple rotors resulting in more complex flow patterns. These flow patterns are no longer approximately symmetrical over the azimuth of the vehicle. On the contrary, the flow is highly dependent of azimuth of vehicle and at certain angles spikes of the local flow velocity can be observed [1][2].

These high velocities can be dangerous for the ground crew and the aircraft. For example, rocks can be picked up and dust can be raised, obscuring the scene (brownout)[3]. Due to the inherent need for urban air taxis to start and land in very densely populated areas further evaluation of the resulting dangers has to be undertaken. For the certification of multirotor aircraft a good understanding of the resulting patterns in the 2D flow plane under real world condition is needed.

To validate the measuring of set outwash, in preparation for the certification of air taxis, the helicopter department at DLR Göttingen is conducting research on helicopters with in ground effect. These studies are conducted on full-scale helicopters in free flight. These experiments have shown that the associated winds speeds of helicopter outwash range from 0 m/s to 50 m/s and that the highest energy fluctuation occur at frequencies below 20 Hz as demonstrated by Braukmann et al. [4]. The aforementioned flow pattern occur in a large area, and can either be measured volumetric or planar, due to concerns of laser safety and complexity, methods like partial tracing velocimetry are not viable.

As a result an array of spacial distributed sensors will be used. The sensor has to be small and cost effective due to concerns of flow blockage and the amount of sensors needed. The majority of heat and momentum based approaches to velocimetry demonstrate a notable reduction in accuracy at air speeds below 5 m/s. For instance, hot wires demonstrate excellent frequency response but exhibit considerable drift over time and poor response to low velocities. This is due to the low forced convection at low wind speeds, which further degrades the accuracy. Cup anemometers exhibit a low over all drift but due to the mechanical inertia of the rotor the frequency response is limited, as well as only being able to measure the magnitude of a 2D flow.

Ultrasonic anemometers represent an attractive solution for this application due to their low complexity and cost. In contrast to impulse and heat based approach to velocimetry, they are exceptionally accurate at measuring very low air speeds.

Commercially available ultrasonic sensors are often costly and can be rather large. Another disadvantage of commercially available sensors is the lack of a synchronization method, which results in uncertainty with regard to the time at which a measurement is taken. This is due to slight clock mismatches of each sensor, which accumulate over time.

The aim of this thesis is to develop a small ( $100\text{ mm} \times 100\text{ mm} \times 100\text{ mm}$ ) and low-cost (about 100€) ultrasonic anemometer. To facilitate integration into the existing measurement system, the sensor will provide an analog output and a method for synchronization. The desired measurements accuracy are in reference of a commercially available Calypso anemometer [5] and are as follows,  $\pm 0.1\text{ m/s}$  at 10 m/s in magnitude and an angle accuracy of  $\pm 1^\circ$  at a sampling rate of 100 Hz.

## 2 Theoretical Background

This chapter will examine the theoretical foundations of the thesis. It will investigate the measurement principle and the basis of the involved signal processing, and possible corrections for measurement errors.

### 2.1 Measurement Principle

The measurement is based on the physical fact that sound pulses propagate through air at the speed of sound. If a difference in speed is measured between two identical signals sent in opposite directions, it can be concluded that the air in which the sound waves traveled has moved. The transmitted sound pulses accumulate this shift throughout the duration of the journey and along the distance traversed. The transmission and reception of ultrasonic pulses are facilitated by the use of transceivers designated A and B, respectively (Figure 2.1). Both transceivers span the measurement path  $l_0$ . In an ideal case, the air speed can be calculated using the following formula:

$$v_{AB} = a + v_{\text{air},AB} = \frac{l_0}{t_{AB}} \quad (2.1)$$

In this context, the variable  $a$  describes the speed of sound, while the variable  $t_{AB}$  represents the time interval between the emission and reception of a signal also known as time of flight (ToF).

Due to the change in the speed of sound caused by external factors such as temperature, humidity and gas composition, a second measurement in the opposite direction is necessary. Assuming a constant airspeed during the measurement, the measured speed can be expressed as follows:

$$\begin{aligned} v_{AB} &= a - v_{\text{air},AB} \\ \iff v_{\text{air},AB} &= v_{BA} - a = \frac{l_0}{t_{AB}} - a. \end{aligned} \quad (2.2)$$

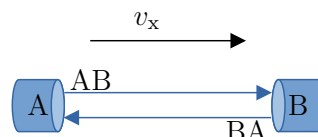


Figure 2.1: The schematic structure of an 1D ultrasonic anemometer

The same formula is valid for the BA transmission

$$v_{BA} = a - v_{air,BA}$$

$$\iff v_{air,BA} = v_{BA} - a = \frac{l_0}{t_{BA}} - a \quad (2.3)$$

under the before mentioned assumption the following is true:

$$v_{air,AB} = -v_{air,BA}. \quad (2.4)$$

The following formula can be used for better noise and error rejection caused by small violations of the aforementioned condition [6]:

$$v_x = \frac{v_{air,AB} - v_{air,BA}}{2} = \frac{l_0}{2} \left( \frac{1}{t_{AB}} - \frac{1}{t_{BA}} \right) \quad (2.5)$$

to acknowledge this difference in measured speed the resulting velocity is denoted  $v_x$ .

The speed of sound can be calculated as follows:

$$\begin{aligned} v_{AB} + v_{BA} &= a + v_{air,AB} + a - v_{air,AB} \\ \iff v_{AB} + v_{BA} &= 2 \cdot a \\ \iff a &= \frac{v_{AB} + v_{BA}}{2} = \frac{\frac{l_0}{t_{AB}} + \frac{l_0}{t_{BA}}}{2} \\ \iff a &= \frac{l_0}{\frac{1}{2}(t_{AB} + t_{BA})}. \end{aligned} \quad (2.6)$$

Note that the above equations only apply when assuming a constant 1D flow along the measurement path. A measurement error will occur if this criterion is not met.

To measure the time between sending and receiving to sub-period accuracy, a matched filter has been selected. A matched filter optimizes the signal-to-noise ratio for a given filter kernel (compare [7]). The matched filter is implemented by cross-correlating a match with the measurement signal. The term “match” refers to a pre-recorded signal that has been captured under optimal conditions.

The shift in the correlation peak in the  $x$ -direction indicates of a time shift exhibited by the signal in comparison to the matched signal. Consequently, the outcome of the filter is a relative delay  $t_{rel}$  to the matched signal. Therefore, the delay  $t_0$  between transmission and reception at the opposite transceiver must be determined for the match. The time required for the matched

signal to traverse the measuring path can be calculated by dividing the distance traveled  $l_0$  by the speed of sound  $a_0$ , assuming that there is no air speed.

$$t_0 = \frac{l_0}{a} = \frac{l_0}{\sqrt{\kappa \cdot R_L \cdot T_0}} \quad (2.7)$$

The total delay between transmission and reception can be readily determined by adding the delay of the matched signal to the relative delay.

$$t_{AB} = t_0 + t_{AB,rel} \quad (2.8)$$

This approach nullifies any offsets due to latency, because both signals experience the same latency and are thus canceled out. Consequently, the temporal alignment of signal transmission and reception must be maintained with precision. Any discrepancy in the timing will inevitably result in an inevitable measurement error. Furthermore, the signals can be cropped, resulting in a shorter signal length, which in turn results in faster computation times.

For the measurement of 2D air flows, at least two 1D measurements in linear independent orientations are required. The velocities measured along the measurement paths are denoted  $v_x$  and  $v_y$  respectively. This can be done with different configurations, in this project the orthogonal configuration is used for simplicity. In an orthogonal configuration (as shown in Figure 2.2), the measurement paths cross at  $90^\circ$  and are located in the same plane. This results in simple trigonometric calculations for the angle  $\alpha$  and magnitude  $v_{mag}$  of the airflow.

The angle and magnitude can be calculated as follows [8]:

$$\alpha = \arctan \left( \frac{v_x}{v_y} \right) \quad (2.9)$$

$$v_{mag} = \sqrt{v_x^2 + v_y^2} \quad (2.10)$$

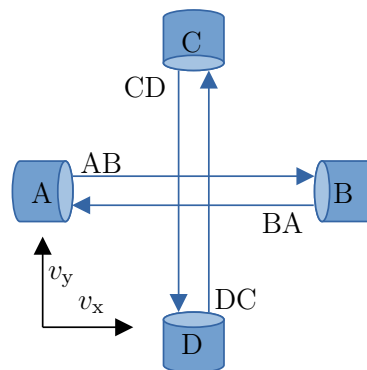


Figure 2.2: The schematic structure of an 2D ultrasonic anemometer

## 2.2 Transducer Shadow

Due to the physical dimensions of the transceiver, the flow is blocked, and thus resulting in a decline in flow velocity due to the exerted drag. This violates the criterion of a constant one-dimensional flow along the measurement path. The impact of this effect is dependent on the angle of the airflow to the measurement path, as well as the geometrical properties of the sensor. One metric for determining the strength of the transceiver shadow effect is the ratio of the measurement path length  $L$  and the diameter of the transceiver  $d$ .

One proposed solution for the problem is the use of a correction function. One solution for non-stream-lined transducers is the use of the Kaimal-Gaynor correction [9]:

$$v_{\text{corr}} = \begin{cases} v_{\text{meas}} \cdot \left( C + \frac{(1-C) \cdot \theta}{75^\circ} \right), & 0^\circ < \theta < 75^\circ \\ v_{\text{meas}}, & 75^\circ \leq \theta. \end{cases} \quad (2.11)$$

Where  $C$  represents the pre-determined correction factor, while  $\theta$  is the angle between the airflow and the measurement path. The measured velocity is denoted  $v_{\text{meas}}$  and the corrected velocity  $v_{\text{corr}}$ . A limitation of this approach is that it assumes a symmetric velocity deficit around the zero-degree mark. For small values of ( $L/d < 20$ ), the correction becomes increasingly inaccurate [10].

## 2.3 Cross-Correlation

Correlation describes the similarity of two given signals. A cross-correlation is a method for evaluating the correlation of two signals over a varying amount of relative shift. For finite, discrete signals, the cross-correlation is defined as follows:

$$(f \star g)_n \equiv \sum_{m=0}^{N-1} \overline{f_m} \cdot g_{(m+n) \bmod N} \quad (2.12)$$

Where  $f$  and  $g$  are finite discrete signals and  $N$  their lengths.

Equation 2.12 is mathematically similar to a convolution. Indeed, it is equal to a complex conjugate convolution, if one of the signals is inverted in the time domain. Given the real-valued nature of the signal, the conjugation can be neglected and, thus, the convolution is equal to the right-hand side of Equation 2.12. Since multiplication in the frequency domain is equivalent to convolution in the time domain, assuming a certain signal length, the transformation to the frequency domain and subsequent multiplication and back transformation are more efficient than calculating the convolution in the time domain. Therefore a common method to accelerate the computation of the cross-correlation is to leverage the previous mentioned equality and utilize convolution.

## 2.4 Phase Shift Keying

Due to the physical inertia of the membrane of the ultrasonic transceivers a sharp single pulse exertion is not possible with the necessary signal strength. It is thus necessary to implement a multi-period excitation of the transmitter in order to ensure optimal signal strength. A simple excitation scheme for the transmitter would yield a highly unambiguous cross-correlation output, as the correlation would be exceedingly high at every shift coinciding with a full period of the sine wave, due to the sine wave-shaped nature of the received signal. In order to obtain an unambiguous filter result, it is necessary to modulate the signal. A signal can be modulated in amplitude, phase, and frequency. However, due to the narrow frequency response band of the transceivers and the inherent shift in amplitude due to the rise and fall in transmission time (and length), neither frequency nor amplitude modulation are viable options. Consequently, a phase shift modulation is selected.

A binary phase shift scheme is used here. The phase shift is executed according to predefined pattern. Phase shift patterns can also be represented as a series of ones and zeros, where zeros describe a phase shift of zero degrees and ones a phase shift of 180 degrees [11]. This pattern may also be referred to as a key. The technique is referred to as phase shift keying (PSK) and is employed in a wide range of wireless communication applications.

## 2.5 Cross Flow Correction

Certain errors can be mitigated by compensation using external factors. For example, by compensating for the increase in ToF caused by the lengthening of the measurement path, due to orthogonal flow can be compensated for. The elongation of the measurement path is a consequence of the ultrasonic pulse being deflected from its intended trajectory by the orthogonal flow, which consequently results in a longer path. The formula for compensation is as follows [6]:

$$a_{\text{corr}} = \frac{a_{\text{meas}}}{\cos(\arctan(|v_{\text{ortho}}|/a_{\text{meas}}))} \quad (2.13)$$

Where  $a_{\text{corr}}$  is the corrected speed of sound and  $v_{\text{ortho}}$  the measured orthogonal velocity.

The error can also be expressed as an elongation of the measurement path  $l_{\text{corr}}$  as a function of the orthogonal velocity  $v_{\text{ortho}}$ .

$$l_{\text{corr}} = l_0 \cdot f(|v_{\text{ortho}}|) \quad (2.14)$$

If the airspeed is sufficiently small compared to the speed of sound, simpler approaches can be used with acceptable error. In this project a second order polynomial is used.

$$l_{\text{corr}} = l_0 \cdot (c \cdot |v_{\text{ortho}}|^2 + b \cdot |v_{\text{ortho}}| + a) \quad (2.15)$$

The corrected distance can be used in the Equations 2.6 and 2.5. The correction of the measurement path yields the important advantage that it also can be used to correct the calculated velocity which is equally impacted by the change in measurement path length.

### 3 Implementation

The design of the sensor can be broken down into abstraction layers: the electrical layer and the software layer. On the electrical layer, components are connected, voltages are converted, and signals are recorded and transmitted. The software layer is responsible for the acquisition and processing of the aforementioned signals. The signal processing can be done either on the microcontroller or on a desktop PC. In order to facilitate this functionality, a USB port has been incorporated into the design. A brief overview over the Sensor IO and of is provided in Figure 3.1. The connection between the PC and the sensor is bidirectional, allowing for the control of the sensor from the PC. The trigger, however, is only capable of functioning as an input.

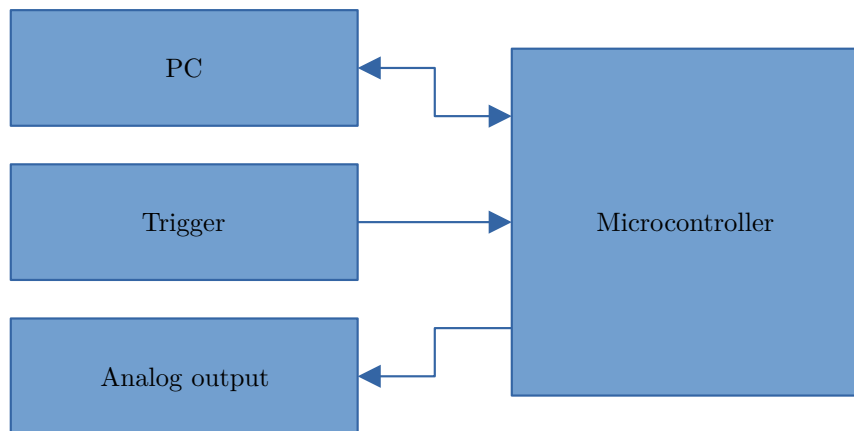


Figure 3.1: Overview over the sensor IO

This approach allows for the analysis of raw data and the comparison of different evaluation methods on the same set of data, utilizing the superior computing power of the PC. Furthermore, the system offers the possibility of numeric optimization and a wide range of graphical analysis methods. In the subsequent chapters, a more detailed explanation will be provided.

#### 3.1 Hardware

The system is divided into distinct components. The central component is the microcontroller, which is a STM32F469. The microcontroller was selected due to its high clock speed and digital signal processing capabilities. The microcontroller serves as the central interface between all other components and is responsible for managing the interaction and their timing.

All electrical components are mounted and electrically connected on a printed circuit board (PCB). For a schematic overview, see Figure 3.2. All depicted sub-components will be described

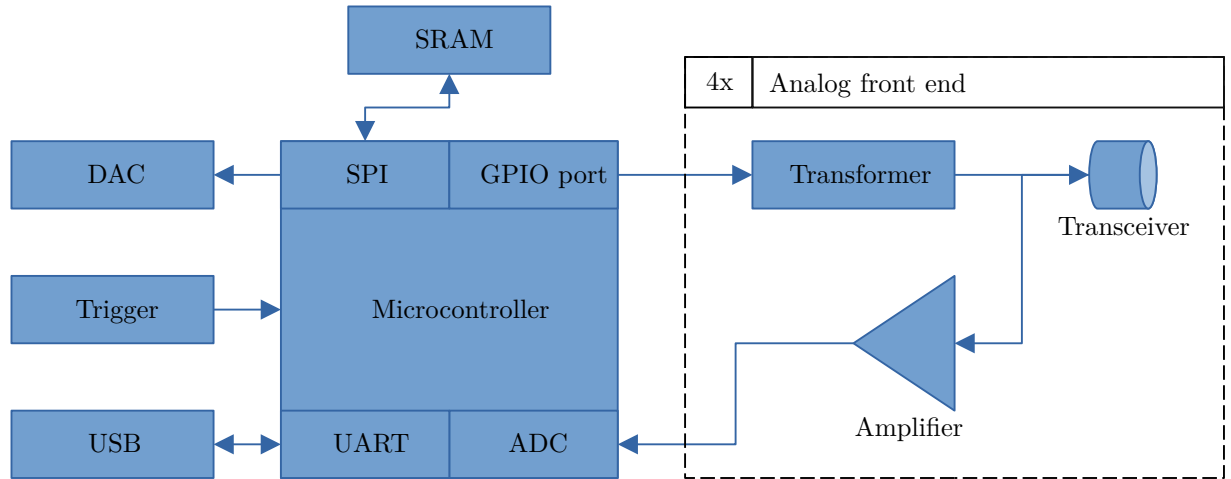


Figure 3.2: A high-level overview of the PCB

in the following paragraphs.

**Analog Front End** The analog front end is responsible for amplifying the input and output voltages of the transceiver to their appropriate voltage levels. The transceiver utilized is a piezoelectric type (UTR-1440K-TT-R) and is designed for 40 kHz transmitting and receiving. In order to transmit ultrasonic pulses, the logic direct current (DC) voltage of 0 to 3.3 V outputted by the microcontroller must be amplified to  $140 \text{ V}_{\text{pp}}$  alternating current (AC) in order to drive the transceiver. The voltage conversion for transmission is achieved through the use of a transformer, which is driven by two MOSFETs, which in turn is switched by the microcontroller.

The received signal exhibits a low amplitude ( $<200 \text{ mV}$ ) and is AC, necessitating conversion to a DC voltage within a range of 0 to 3.3 V for proper conversion of the analog voltage to a digital signal by the microcontroller. In order to achieve this, a two-stage amplifier with an AC-to-DC conversion circuit is employed. The analog-to-digital converter (ADC) of the microcontroller samples the signal at 800 kHz and converts each sampled voltage into a 12-bit integer.

It is essential that the driving of the MOSFETs and the ADC conversion of the received signal are closely coupled in order to minimize the noise in the measured data. Such jitter would result in a measurement error in the final result. In order to achieve this, both peripherals are linked to the same microcontroller timer.

**USB Interconnect** To transmit data from the microcontroller to the PC, a USB interface is utilized. The conversion of the asynchronous serial interface (UART) of the microcontroller to the USB interface is managed by an FT231 IC. This combination allows for a baud rate (transmission rate) of 1 Mbaud. A checksum (CRC32) is essential for verifying data integrity of the transmission and must be calculated and transmitted with each transmission. The limiting factor of the transmission throughput is not the actual limit in baud rate, but rather the calculation of the checksum.

**SRAM** Due to this limitation in data transmission throughput, an external RAM IC was incorporated. The aforementioned limitation would restrict the measurement frequency of the sensor in the USB transmission mode. In particular, the use of high frequencies is of great interest when analyzing phenomena such as cross-talk or poor transmitter dampening. This is due to the fact that these phenomena are more likely to occur at high frequencies when the time between sending and receiving is smaller.

The external RAM allows for the storage of a large number of measured signals at high speeds. The RAM-IC is connected via a serial peripheral interface (SPI), which allows for much higher transmission speeds than the USB interface. This enables the recording of a batch of measurements at high speeds and their subsequent transmission to the PC via USB. In this operational mode, the measurement frequency can reach up to 300 Hz.

**Digital-to-Analog Converter** In order to establish a connection between the sensor and the analog measurement system of the DLR, a 2-channel 14-bit high-accuracy digital-to-analog converter (DAC) is utilized (AD5732AREZ). This device is responsible for converting the digital measurement value into an analog voltage range between  $-10$  and  $10$  V. In order to achieve greater accuracy, an external voltage reference (REF3425TIDBVR) and a separate ground plane are employed. The DAC is connected to the microcontroller via the SPI. Additionally, the DAC is linked to the trigger input, enabling the DAC update to be initiated automatically by the trigger signal. In order for this to occur, the microcontroller must first pre-write the next output value to the DAC, without updating the DAC's output register. This DAC update can be triggered either by the microcontroller or the trigger input.

**Trigger** In order to synchronize the sensors, a trigger input is utilized in this design. The trigger input is connected to the microcontroller via an interrupt-capable GPIO pin of the microcontroller. Consequently, if the trigger exerts a predefined behavior (for example, a rising or falling edge), an interrupt is called. This interrupt causes the main program to stop its execution and instead execute a different, previously defined section of code that handles the interrupt. This previously defined section of code, resets the inner system tick timer, synchronizing every sensors inner time source.

**Mechanical Construction** The mechanical construction of the device comprises the main body, the main PCB, and the transceivers, which are mounted to a PCB. The main body is comprised of 3D print, which enables the integration of all components and the presentation of potential mounting options. A 3D print was chosen because of the low manufacturing cost and high design flexibility as well as for the low transmission of structure-borne noise. The primary PCB serves to house all of the aforementioned electronic components and facilitate the interconnection of all electrical systems.

As illustrated in Figure 3.3, the sensor has a measurement path of  $d = 60$  mm and the transceivers have a diameter of  $L = 14.4$  mm, resulting in a  $L/d$  ratio of 4.16. The overall dimensions of the

sensor are  $100\text{ mm} \times 100\text{ mm} \times 100\text{ mm}$ . The sideways offset of the transceivers is 2.8 mm which is a result of the mounting of the transceivers to the PCB.

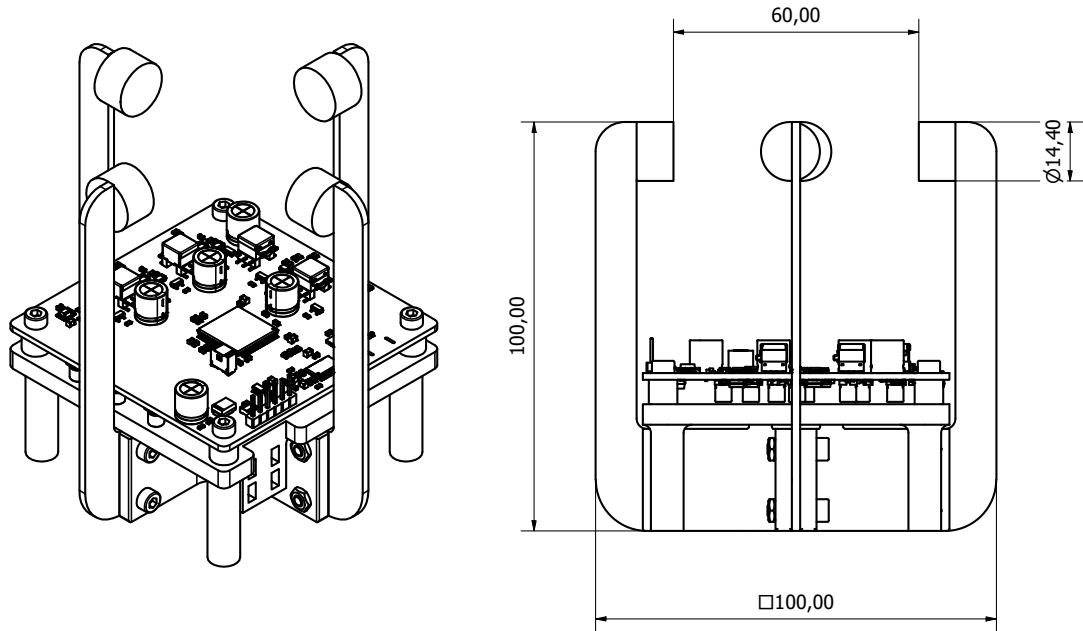


Figure 3.3: An iso-metric view of the sensor and its dimensions

## 3.2 Software

The software can be divided in into different parts, the data acquisition side and the data processing side. The data acquisition depends on whether the data should be processed on the microcontroller or on the PC.

### 3.2.1 Data Acquisition

This subsection is dedicated to the exact implementation of the sending and receiving of the signals. If the signal processing takes place on the PC, the received data is stored in the RAM and later transmitted to the PC.

#### Sending and Receiving

As previously stated in Chapter 2, it is of importance that the sender and receiver have an exact and repeatable timing. This is achieved by writing the GPIO-Pin output register and triggering

the data acquisition with a DMA controller. The DMA controller is capable of transferring data between peripherals without the involvement of the CPU. This allows the CPU to continue executing other code, and that the data transfer is not influenced by the current state of the CPU. The DMA controller is internally triggered by a timer, which is capable of repeatedly and constantly triggering the transfer of data.

It is necessary for the DMA controller to be configured and activated by the CPU at each query start separately. Consequently, for a single measurement, all four transceiver data queries must be initiated. The query pattern is as follows: AB, CD, BA, DC.

The data transfer occurs at a frequency of 800 kHz, which corresponds to 20 ADC samples per period of the 40 kHz transceiver signal. The recording length is 632 samples. In order to account for the approximate delay between the transmission of the ultrasonic pulses and their reception, the sending buffer is padded by 120 samples at the beginning of the recording. Consequently, only 512 samples of the relevant sections of the signal undergo further processing.

### Key Pattern

In order to transmit the ultrasonic pulses via DMA, a GPIO output pattern is required. This pattern must be pre-generated and is unique for each transceiver. Each transceiver is driven by two MOSFETs, which are alternately switched. These are referred to as switch 1 and switch 2. The pattern is comprised of an array of 16-bit unsigned integers, which can be directly written to the 16-bit wide GPIO output registers. Each bit represents a GPIO pin and its output state. To generate the pattern, the phase shift key and the data increment per period must be known. To generate the key pattern, an array of zeros is first created, with the length of the key multiplied by the number of increments per period. The pattern is then filled on a period-by-period basis, with the key position incremented after each period.

If the current key position is equal to zero, then the bits corresponding to the GPIO pin connected to switch 1 of the transmitter are set (set = 1) in the first half of the period, and the second half is filled analogously with the bit for switch two. If the current key position is equal to one, then switch 1 and 2 are exchanged. In order to conserve power, it is possible to set each pin for only half or a third of the period. This will not significantly alter the amplitude. Certain sub-period driving patterns may be employed, which can influence the achieved output waveform.

The optimal key is not easily calculated or read up on. The differences between the characteristics of the various transceivers models are quite significant, which makes it difficult to determine a single key that is suitable for all transceivers. One possible approach to finding a suitable key is to try all keys at a certain key length and observe the respective filter output. This can be easily accomplished through the use of a script. The primary criterion for evaluating the key is the ratio of the primary peak in the filter output, while the secondary criterion is the amplitude of the signal. In order to compensate for the signal strength loss that occurs at higher air speeds due to the longer signal run time and higher distortions caused by fluctuations in the air flow,

the signal must exert a certain amplitude in order to guarantee an unambiguous filter result. The key in question is 12-bit long and has the key values of 0, 1, 1, 1, 0, 0, 0, 1, 0, 1, 1, 0.

### 3.2.2 Data Processing

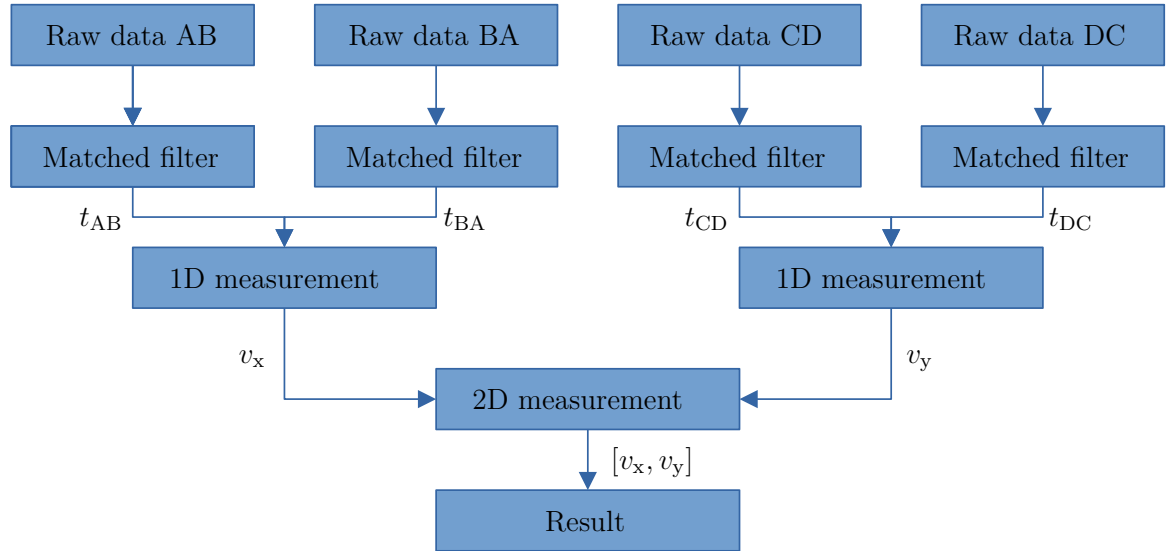


Figure 3.4: Overview of the signal processing steps

A brief overview of the data processing process is given in Figure 3.4. The process can be divided into 3 stages: filtering, 1D measurement, and 2D measurement. Each stage reduces the amount of data. As shown in Figure 3.4 the filter converts the raw data in to a list of potential delays which intern get converted in to a list 1D measurement. In a final step both 1D measurement get combined to a 2D measurement.

#### Filtering

The theory of the matched filter is described in Chapter2. This chapter focuses on the implementation and concrete evaluation of the filter. The input of the filter is the raw data from one of the transceivers. The output of this section is a set of peak data with a corresponding likelihood score.

In theory, the main peak of the correlation should correspond to the measured relative delay of the signal to the match, but in practice, due to signal distortion, the filter peak can be ambiguous. When the amount of signal distortion is high, the ambiguity of the filter increases and the difference in height between the main peak and its neighbors diminishes. The primary peak ratio (PPR) is used as a metric to judge the ambiguity of the filter. The PPR describes the ratio of the main (highest) peak amplitude to the amplitude of the regard peak. This ratio is stored in a score variable that is later used to identify the solution with the highest probability of being correct.

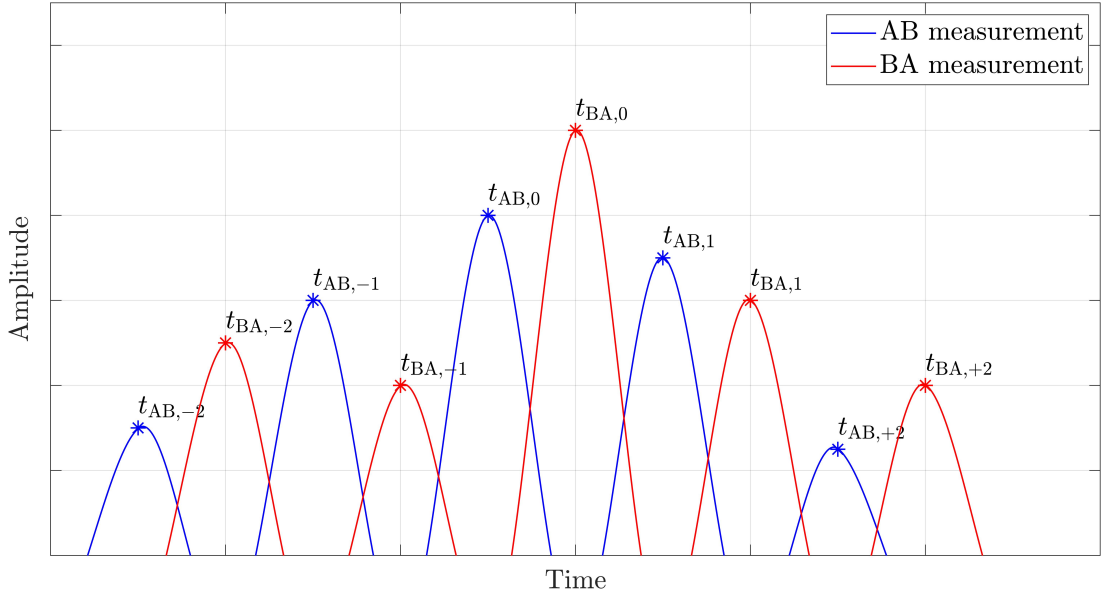


Figure 3.5: Schematic filter output with peaks marked

Peaks are denoted with the index of their measurement path and their relative position to the primary peak (see figure 3.5).

To enhance the measurement accuracy, the neighboring points of the peak are used to fit a parabola to peak, and determining the maximum of said parabola, gaining sub-period accuracy. Subsequently the peaks  $x$  position (which is in ADC sample time) is converted to a relative delay.

Preliminary tests have shown that the peak corresponding to the real relative delay can be shifted up to two peaks to the left or right of the main peak. To further evaluate the measurement, all five relative delays corresponding to the peaks are passed to the next processing step.

## 1D Measurement

In this step, two filter outputs are combined to a 1D measurement of velocity and speed of sound, the three most likely candidates pass to the next step. To evaluate the probability of the candidate, a new score is built with the score of the previous step and the discrepancy to a reference speed of sound.

Both filter outputs consist of five relative delay value candidates. These candidates can be represented in a  $5 \times 5$  matrix:

$$T = \begin{bmatrix} t_{-2, -2} & t_{-2, -1} & t_{-2, 0} & t_{-2, +1} & t_{-2, +2} \\ t_{-1, -2} & t_{-1, -1} & t_{-1, 0} & t_{-1, +1} & t_{-1, +2} \\ t_{0, -2} & t_{0, -1} & t_{0, 0} & t_{0, +1} & t_{0, +2} \\ t_{+1, -2} & t_{+1, -1} & t_{+1, 0} & t_{+1, +1} & t_{+1, +2} \\ t_{+2, -2} & t_{+2, -1} & t_{+2, 0} & t_{+2, +1} & t_{+2, +2} \end{bmatrix} \quad (3.1)$$

with:

$$t_{i,j} = \frac{t_{AB,i} + t_{BA,j}}{2}.$$

Not all 25 combinations need to be evaluated, because for some combinations the mean relative delay will not change significantly. Which means that the calculated speed of sound will not change by a noteworthy amount (see Equation 2.6). This is due to peaks being shifted symmetrical relative shift to the mean. For example the measurement  $t_{0,0}$  has the same mean relative delay, as  $t_{-1,1}$  and  $t_{1,-1}$  because the left shift (smaller delay) of one is canceled out by right shift(larger delay) of the other. This phenomena can be noticed along diagonals parallel to  $t_{-2, +2}$  to  $t_{+2, -2}$  line. These are diagonals of (nearly) constant speed of sounds Thus the matrix can be reduced to a vector of nine unique combinations:

$$T_{\text{reduced}} = \begin{bmatrix} t_{-2, -2} \\ t_{-2, -1} \\ t_{-1, -1} \\ t_{-1, 0} \\ t_{0, 0} \\ t_{0, +1} \\ t_{+1, +1} \\ t_{+1, +2} \\ t_{+2, +2} \end{bmatrix} \quad (3.2)$$

The speed of sound is calculated for all combinations of  $T_{\text{reduced}}$ . The three combinations with the smallest difference to the speed of sound are selected.

All peak combinations on the diagonal of constant speed of sound (of the chosen speed of sound) of the matrix result in the same average delay, so to decide which combination to choose (form the particular diagonal), a score is calculated for each combination along this diagonal. The score is calculated by adding the two relative delay scores of the peak candidates together.

$$s_{x,n} = s_{AB,i} + s_{BA,j}$$

The value of the combination with the lowest score are passed to the next step. This step is performed for the  $y$ -measurement data analogously.

Should the filter output become ambiguous, there is a possibility of a misinterpretation of a main peak occurring. This shift would result in a significant error, which can easily be detected, for example, a shift of one peak to the left or right would result in a change of 50 m/s in the speed of sound, which would internally correspond to a temperature change (assuming ideal gas and no change in gas composition) of over 70 K. A temperature change of such magnitude would exceed the rated temperature of the sensor, and is unlikely to occur spontaneously. This high jump in air temperature is unlikely to occur spontaneously, thus this criterion has been selected.

## 2D Measurement

In this step, both 1D measurements are combined into a 2D measurement and compensated for cross-flow.

First the correction factors  $l_{corr,x}$  and  $l_{corr,y}$  are calculated via the polynomial correction method detailed in Equation 2.15. After applying the correction, to the speed of sound candidates,  $a_y$  and  $a_x$  correspondingly. The result can be interpreted as two  $3 \times 3$  matrices with different speeds of sound. Then the fact is leveraged that, both sound speeds are expected to converge towards each other [6].

$$A_x = \begin{bmatrix} a_{x,1} \\ a_{x,2} \\ a_{x,3} \end{bmatrix} \cdot \begin{bmatrix} l_{corr,y,1} & l_{corr,y,2} & l_{corr,y,3} \\ l_0 & l_0 & l_0 \end{bmatrix} \quad (3.3)$$

The matrix  $A_y$  is calculated with indices  $x$  and  $y$  swapped.

The score is construed in such a way that aforementioned convergence of the speeds of sound as well as the convergence to the speed of sound of the previous measurements is evaluated.

$$S_a = |A_x - A_y| + \left( \left| \frac{A_x + A_y}{2} - a_{ref} \right| \right) \quad (3.4)$$

$$S = S_a \cdot w + S_{peak} \quad (3.5)$$

$S_{peak}$  is calculated as follows:

$$S_{peak} = \begin{bmatrix} s_{x,1} \\ s_{x,2} \\ s_{x,3} \end{bmatrix} \cdot \begin{bmatrix} s_{y,1} & s_{y,2} & s_{y,3} \end{bmatrix} \quad (3.6)$$

Where  $s$  is the calculated score from the previous 1D measurement step.

The combination with the lowest score is selected. After this step, the velocity corresponding to the chosen candidate is calculated, using the corrected distance and output.

### 3.2.3 Triggering

To achieve synchronization of the sensor, a trigger is employed, which interrupts the program at a rising edge of an external periodic signal. The aforementioned signal can be generated, for instance, by a function generator.

At a rising edge of the trigger a new measurement is started. The number of measurement samples taken and their distribution in time can be pre-configured via a terminal accessible via the USB to serial interface. After all measurement samples are collected, the data is filtered with a configurable filter (min, max, median, mean) and outputted by the DAC.

## 4 Calibration, Correction, and Validation

The following chapter will describe the experimental setup, which is used to create the data sets later used. These data sets are then employed to calibrate and validate the sensor data. The resulting measurements will be examined, and strategies to mitigate the measurement error will be evaluated.

### 4.1 Experimental Setup

To calibrate and validate the sensor, it is tested in a wind tunnel of the DLR site in Göttingen (Schallarmes Labor Göttingen (SAG)), which can reach speeds of up to 45 m/s and is padded with sound-absorbing foam.

The sensor is mounted on a pole, which in turn is mounted on a rotating table with a scale for measuring the angle. A DANTEC low speed precision anemometer is used for reference measurements, as well as a Prandtl tube for dynamic pressure measurements. For reference speeds below 10 m/s the DANTEC anemometer is used, for higher speeds the dynamic pressure measurement of the Prandtl tube is used to calculate the reference air speed.

Both sensors are placed so that their readings are not influenced by the ultrasonic anemometer (see Figure 4.1). All of the above components are mounted on an X95 truss structure, which is placed in the open test section of the wind tunnel (see Figure 4.2). A PT100 thermometer and a barometer are used to determine the temperature and static pressure of the air, needed to derive the reference air speed from the dynamic pressure measurement of the Prandtl tube.

Each test case of the measurement campaign consists of 400 2D measurement samples recorded at 100 Hz, unless otherwise noted.

### 4.2 Calibration of Velocity Offset and Magnitude

To calibrate the sensor, measurement points at 45°, 135°, 225°, and 315° are used. These angles are chosen because the blockage of the flow is low and the influence of any disturbances should occur equally on each measurement path.

The correction scheme is as follows:

$$v_{\text{corr}} = \begin{cases} (v_{\text{meas}} - v_{\text{off}}) \cdot c_+, & 0 \leq v_{\text{meas}} \\ (v_{\text{meas}} - v_{\text{off}}) \cdot c_-, & v_{\text{meas}} < 0 \end{cases} \quad (4.1)$$

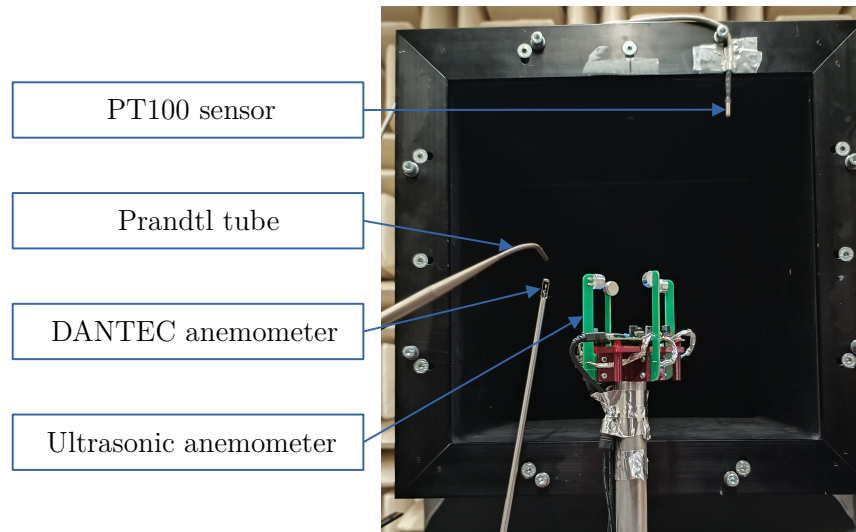


Figure 4.1: Placement of the sensors in the measurement setup



Figure 4.2: Overview of the measurement setup

The distinction between the negative and positive sign is implemented to mitigate the slight change in linearity of both signals, and achieve symmetry important for the mapping the measurement points across the azimuth.

In the first step, the zero offset is calibrated by recording a measurement in absolute still air. This offset is later subtracted from each velocity component. The velocity offset should be zero, as the match signal was also taken under no airspeed conditions. Therefore, the change in relative delay (resulting in the velocity offset) is solely due to the change in speed of sound between the recording of the match and the calibration.

In the second step, the velocity magnitude is calibrated by calculating the mean of the positively signed velocities  $v_{+,m}$  at each reference air speed (analog for negatively signed velocities). So that for each reference air speed there is one  $v_{+,m}$  and  $v_{-,m}$ . The coefficient is calculated using the following formula:

$$c_+ = 1/N \cdot \sum_{n=1}^N \frac{(v_{\text{ref}})_n}{|(v_{+,m})_n|} \quad (4.2)$$

$$c_- = 1/N \cdot \sum_{n=1}^N \frac{(v_{\text{ref}})_n}{|(v_{-,m})_n|} \quad (4.3)$$

In this context, the symbol  $n$  represents the index of the reference speed, while the symbol  $N$  denotes the total number of reference speeds used.

The calibration is calculated for each measurement path and applied to all measurements. In the following analysis it is assumed that this calibration is sufficient and that the sensor measurements are point symmetrical due to the point symmetrical placement of the transceivers, allowing the mapping of data from a quadrant over the whole azimuth of the sensor.

### 4.3 Correction for Elongation of the Measurement Path

The measurement path is elongated, due to orthogonal flow. This elongation can be compensated for by utilizing the velocity measurement along the orthogonal measurement path. This elongation can be readily observed through a decrease in the perceived speed of sound. The reduction in the speed of sound is proportional to the change in measurement path length, as demonstrated by Equation 2.6. This phenomenon allows for compensation to be carried out using the perceived speed of sound at different speeds. The coefficients of the second order polynomial (compare Equation 2.15) are determined by fitting the polynomial to the inverse change of speed of sound perceived by the sensor.

#### 4.4 Statistical Error

The data presented in Figure 4.3 represents the empirical standard deviation across the angles  $0^\circ$  to  $350^\circ$ , recorded in  $10^\circ$  increments. The standard deviation is displayed on the radial-axis, while the angle of the sensor to the inflow is displayed on the  $\theta$ -axis. Notable peaks are evident at specific angles, which could be considered approximately point symmetric. The lack of symmetry at the  $45^\circ$  mark may be attributed to the offset mounting of the transceivers. Given this evidence, further discussion will focus on one quadrant. The peaks are situated between  $30^\circ$  and  $50^\circ$ , and the peaks are offset by a multiple of  $90^\circ$ . The amplitudes of these measurements are approximately twice that of the measurements taken at  $0^\circ$ ,  $90^\circ$ ,  $180^\circ$ , and  $270^\circ$  degrees. During the rotation of the sensor in the air stream, an audible change in sound was observed. This phenomena can be attributed to to a periodically accruing vortex shedding.

In a preliminary testing using a 1D ultrasonic anemometer, it was found that the highest standard deviation is expected at  $0^\circ$ . This peak in standard deviation is attributed to the turbulent wake of the transceiver. A significant distinction between the two sensors is the  $L/d$  ratio. The sensor utilized in the preliminary test has a  $L/d$  ratio of 15.28, while the new sensor has a  $L/d$  ratio of 4.17.

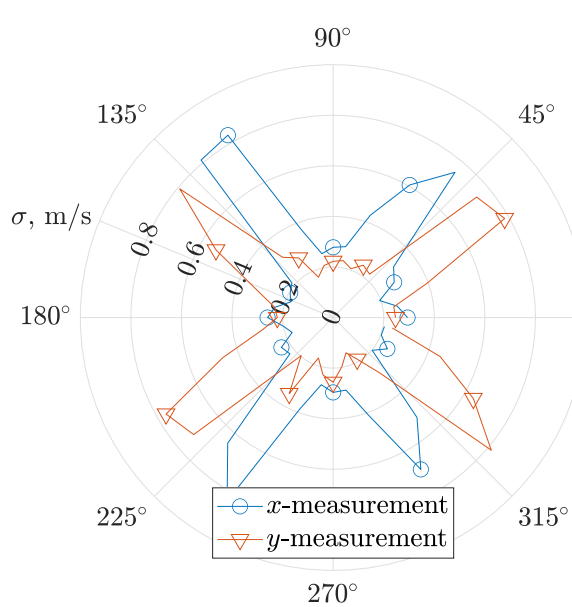


Figure 4.3: Standard deviation across the angles

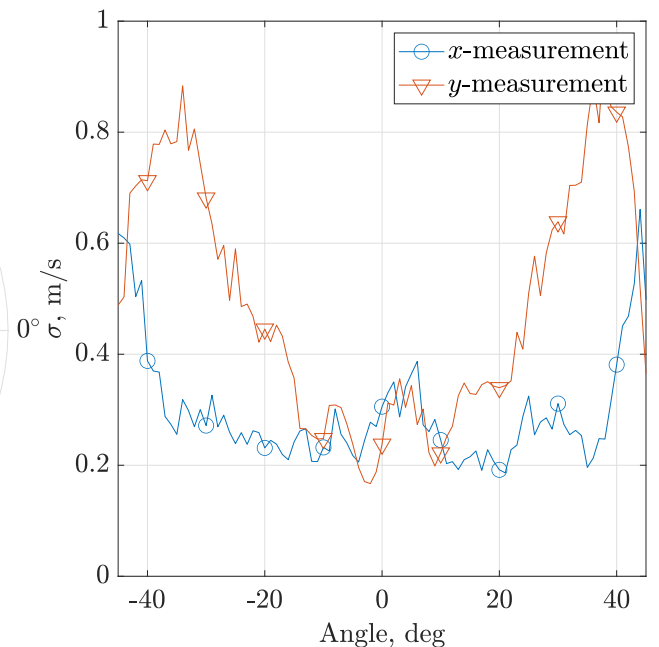


Figure 4.4: Standard deviation across a quadrant, fine resolution

Figure 4.4 illustrates the empirical standard deviation as a function of angle, with measurements taken at increments of  $1^\circ$  between  $-45^\circ$  and  $45^\circ$  at a velocity of  $20\text{ m/s}$ . In this instance, only 100 measurements samples were taken. The standard deviation is displayed on the  $y$ -axis, while the angle of the sensor to the air stream is displayed on the  $x$ -axis. For the  $y$ -measurement, the minimum standard deviation is observed at  $-2^\circ$  and  $0.147\text{ m/s}$ , while the maximum standard

deviation is measured at  $38^\circ$  with a value of  $0.857 \text{ m/s}$ . The maximum measured standard deviation is 5.83 times greater than the minimum measured standard deviation. It reaches a maximum at approximately  $-30^\circ$  and  $38^\circ$ , after which it declines, resulting in a reduced standard deviation between  $-20^\circ$  and  $20^\circ$ .

The standard deviation of the  $x$ -measurement exhibits an increase around the angles of  $-45^\circ$ ,  $0^\circ$ , and  $45^\circ$ , yet remains at a comparatively low level.

The overall change in standard deviation across the angle appears to be gradual. This suggests that there are no intermediate angles with significantly higher standard deviation than that observed in the Figure 4.4.

Figures 4.5 and 4.6 illustrate the data collected at angles between  $-45^\circ$  and  $45^\circ$  at  $5^\circ$  intervals and at various reference air speeds. Figure 4.5 displays the empirical standard deviation the  $y$ -axis in  $\text{m/s}$ , while the angle of the sensor to the air stream is displayed on the  $x$ -axis. Figure 4.6 presents the overall mean of the standard deviation between the angles at a given velocity. The mean standard deviation exhibits a approximately linear trend. The measurement in the  $x$  direction demonstrates a lower mean standard deviation across the whole velocity regime. Thus the following discussion will focus on the  $y$ -measurement.

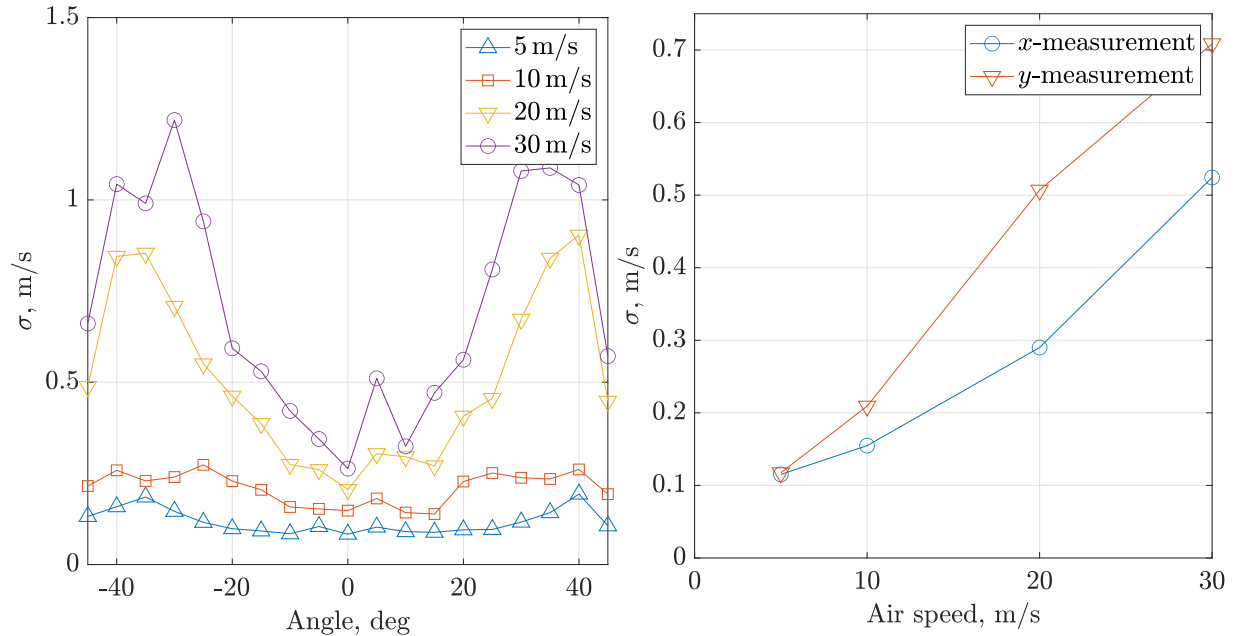


Figure 4.5: Standard deviation of the  $y$ -measurement across angles  $-45^\circ$  to  $45^\circ$  at different air speeds

Figure 4.6: Mean standard deviation across angles  $-45^\circ$  to  $45^\circ$  across velocity, for  $x$ - and  $y$ -measurements

Figure 4.5 displays the various standard deviations at specific speeds across the angle. The overall trends differ significantly between the measurements taken at  $5 \text{ m/s}$  and  $10 \text{ m/s}$ , to the measurements at  $20 \text{ m/s}$  and  $30 \text{ m/s}$ . At the angles between  $30^\circ$  and  $40^\circ$  degrees and between

$-40^\circ$  and  $-30^\circ$ , a distinct peak in standard deviation is observed at air speeds greater than  $20\text{ m/s}$ , with the value of the error doubling at these points. For velocities below  $20\text{ m/s}$ , this feature is not as distinctly present, and the standard deviation is nearly constant and at an overall low level. The data presented in Figure 4.5 suggests that at air speeds exceeding  $20\text{ m/s}$ , other error causes dominate the overall measurement noise at certain angles. These discrepancies can be attributed to a reduction in signal amplitude, which subsequently results in a deterioration of the signal-to-noise ratio. This in turn result in errors in the signal processing. It is similarly conceivable that aerodynamic effects become significant at air-speeds and certain angles exceeding  $20\text{ m/s}$ , affecting the measurement accuracy.

The frequency analysis of the measured velocities does not demonstrate a disproportionate impact of certain frequencies in the measured signal. The majority of the error appears to accumulate over the frequency range. This leads to the conclusion that the measurement error is either predominantly due to signal processing errors or that the frequency of the disturbance is at an even higher frequency (or is not periodic). Due to the Nyquist criterion the maximum predictable frequency of the sensor is  $50\text{ Hz}$ .

The notable alteration in auditory perception when rotating the sensor in the air stream indicates that the observed discrepancy in the measurement may be attributed to a changing aerodynamic effect in the measurement plane. The propagation of sound waves through highly turbulent air can result in the pulses being “blown off course”, which consequently causes a lengthening of the measurement path of the pulse. Due to the time between both transmissions the effect may only be significant for one of the two transmissions. The aforementioned phenomenon, which is not accounted for and exhibits irregular lengthening of the measurement path, will inevitably result in a measurement error. The magnitude of this effect is likely to be amplified by the sensor’s exceedingly low  $L/d$  ratio and the transceiver’s aerodynamically blunt body.

Figure 4.7 depicts the mean subtracted distribution of delays  $t_{CD}$  and  $t_{DC}$  measured along the  $y$ -measurement path in opposite directions. On the  $y$ -axis of the histogram, the normalized (by sample count) occurrences are displayed and on the  $x$ -axis the deviation to the mean delay. The figures were generated on the same data bases as the aforementioned results. Figure 4.7a depicts the delay distribution for the measurement at  $0^\circ$  and Figure 4.7b for the measurement at  $-35^\circ$ . The distributions displayed in Figure 4.7a are approximately normal distributed, the orange  $t_{DC}$  distribution is broader than the blue  $t_{CD}$  distribution and features a less pronounced peak. The broader distribution means a less accurate measurement or speaking in terms of the normal distributional a higher standard deviation. In contrast, the distributions displayed in Figure 4.7b are not normal distributed and feature more than one peak. The distinct double peak nature could indicate an alternating vortex detachment called Karman vortex street and is caused by a upstream transceiver, which would result in an periodically changing velocity field in the measurement path, causing as sort of transceiver vortex effect. It is probable that this error is amplified by the low  $L/d$  ratio and the subsequent reduction in the distance of the upstream transceiver from the orthogonal measurement path. Consequently, the vortex has does not decay

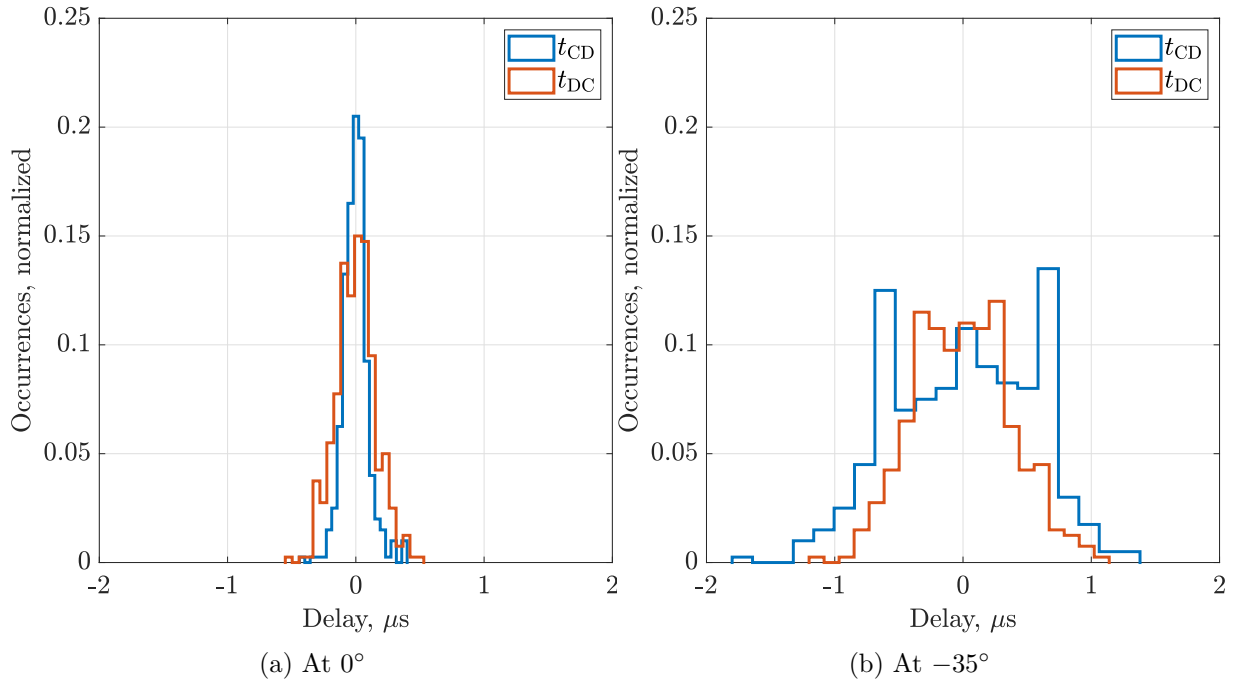


Figure 4.7: Measurement distribution, across delay divergence from mean delay, at 20 m/s

over the short distance, resulting in a proportionately large section of the measurement path being affected by the disturbance. The blue  $t_{CD}$  distribution is over all broader than the orange  $t_{DC}$  distribution. This is due to the longer over all traveling time of the CD transmission and thus a higher error can accumulate over time.

The frequency analysis of the  $t_{CD}$  data, resulted in a distinct peak at 28 Hz, not corresponding with the empirical predicted vortex shedding frequency of around 280 Hz.

Should the perceived measurement error be a consequence of an ADC sample shift, it would manifest as a sudden change in the relative delay of approximately 1.25  $\mu$ s. It can thus be concluded that the time error is not attributable to a raw signal shift in the signal processing.

There are multiple viable approaches to resolving or minimizing the magnitude of this effect. One such approach is to filter the signal in order to reduce the measurement error. Alternatively, the measurement plane can be tilted in order to limit the interaction of the transceiver wake with the measurement. A third potential approach would be to modify the transceiver geometry with the objective of enhancing its aerodynamic properties. However, this has not been demonstrated to yield a measurable improvement in the resulting measurements.

The data presented in Figure 4.8 (a and b), represent the filtered data from 4.5. Two filters were applied over a filtering window comprising five measurement samples. On the  $x$ -axis the angle is displayed while on the  $y$ -axis the empirical standard deviation is displayed.

In Figure 4.8a a mean filter was applied (also referred to as a moving average), whereas in Figure 4.8b, a median filter was utilized. The filter window is 5 samples long.

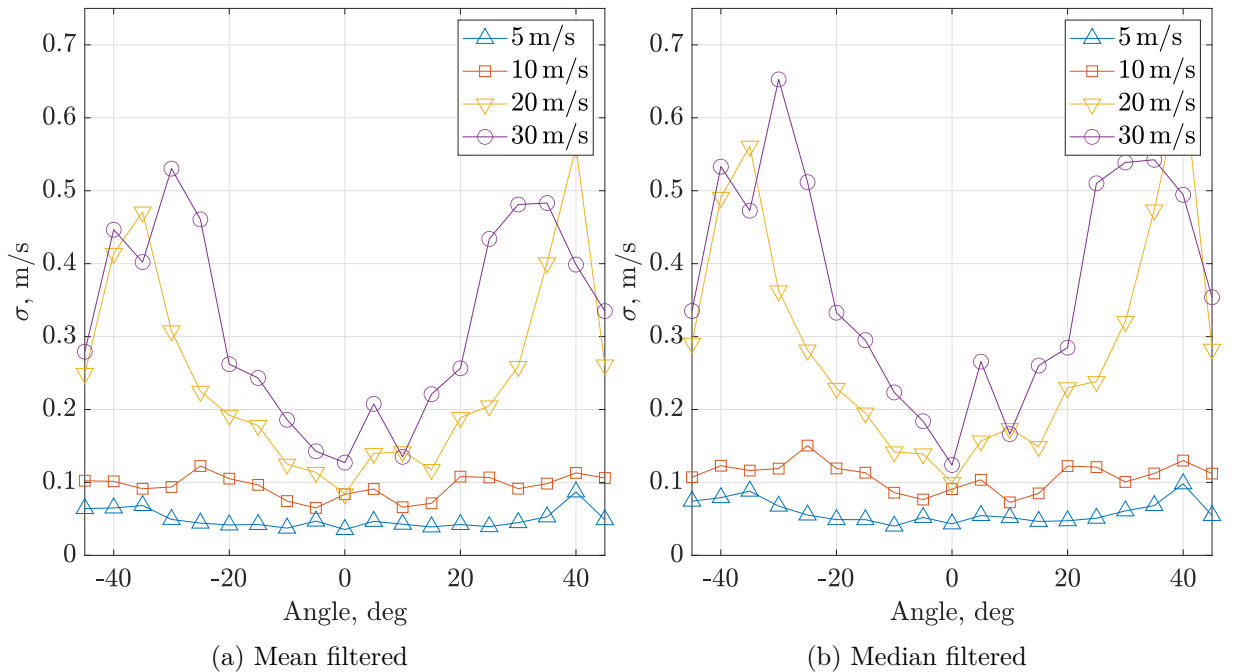


Figure 4.8: Standard deviation across a quadrant, with different filters

The overall trend of the curves displayed in Figure 4.8 are roughly the same as the curves presented in Figure 4.5. The application of the filter results in a noticeable improvement in standard deviation. It is noteworthy that the degree of improvement varies across the curves. While the maximum deviation measured at 30 m/s decreased approximately by a factor of two, the deviation recorded at smaller reference velocities did not undergo a similar reduction. This is contrary to the expectation that all curves should be impacted roughly equally by the filtering. This could lead to the conclusion that the underlying error distribution or the dominating error cause changes. It is debatable whether the overall improvement in the standard deviation is worth the reduction in predictability and/or loss of sampling rate.

Figure 4.9 displays the mean and max empirical standard deviation, displayed on the  $y$ -axis to the filter window size on the  $x$ -axis, for median and mean filter. This analysis is based on the same data set as the previous discussions. Both median and mean filter follow the same overall trend of a declining empirical standard deviation over a raising window size. The improvement gain per additional sample is especially high for small window sizes. The curve flattens significantly after around a window size of 30 samples. The improvement in standard deviation, with rising filter window sizes, is more pronounced on the maximum deviation as it is on the mean deviation. The mean filter has a lower mean and maximum deviation than the median filter across the entire filter window size range. Thus for minimizing the standard deviation a mean filter should be chosen.

An alternative approach would be to tilt the sensor in order to reduce the impact of the transceiver wake on the measurement path. This approach is applicable only if a main flow direction is known

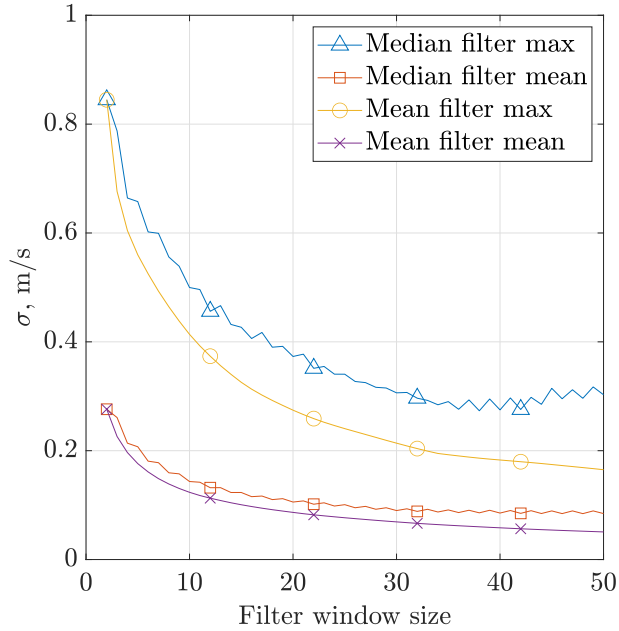


Figure 4.9: Mean and max standard deviation over filter window size

and the sensor can be tilted into the direction of the main flow. An error will be introduced because the flow cannot be considered two-dimensional. This error is a result of cross flow, part of the error can be mitigated by approximating the resulting orthogonal velocity component. Another down side is the need for coordinate transformation to compensate for the angle of the sensor. It has been observed that a tilting of the sensor by  $15.5^\circ$  in the main flow direction results in a notable enhancement in the error statistic at the critical angles.

Nevertheless, due to the described disadvantages, which cannot be readily compensated for, the use of this approach is not recommended.

#### 4.5 Velocity Correction

Figure 4.10 shows the mean measured  $x$  and  $y$  velocities over the angles  $-5^\circ$  to  $95^\circ$  at different reference air speeds in red. The black graphs are calculated speeds represent the expected values. The reference air speeds are  $5\text{ m/s}$ ,  $10\text{ m/s}$ ,  $20\text{ m/s}$  and  $30\text{ m/s}$ . The data was collected between  $-45^\circ$  and  $45^\circ$  and later mapped into one quadrant, assuming the data is as point symmetric as the sensor.

For small angles, the  $x$ -measurement (Figure 4.10a) exhibits a high velocity deficit caused by the transceiver shadow effect (blocking of the flow by the transceiver and the subsequent decline of air speed). By rotating the  $y$ -measurement path by  $90^\circ$ , the occurrence of the transceiver shadow effect is shifted by  $90^\circ$ . The total range of angles at which the transceiver shadow effect occurs is large. The measured air speeds across the  $x$ -measurement path, is approximately linear decries between  $50^\circ$  to  $95^\circ$ . At  $75^\circ$  a non-symmetrical dip in the measured  $y$ -velocity occurs (see Figure 4.10b). This dip is not mirrored as strong in the  $x$ -measurement. This effect is caused by the

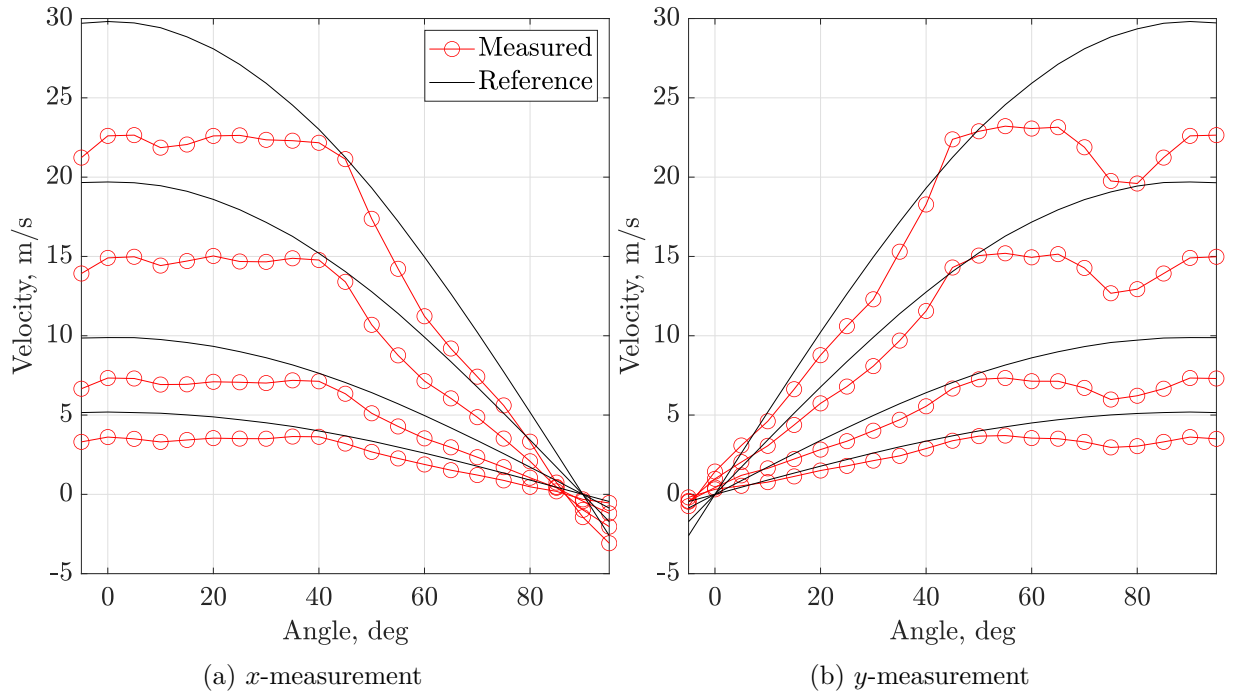


Figure 4.10: Measured and reference values across a quadrant

offset mounting of the transceivers. In particular, the zero crossings of the measured velocities are not at  $90^\circ$  and  $0^\circ$  respectively, but are shifted by about  $2.5^\circ$ .

Due to the aforementioned dip, the resulting function of the red graphs lacks an unambiguous inverse function. This prompts the question of whether the correction is unambiguously solvable or if certain points exist with multiple solutions. Figure 4.11 depicts two velocity component planes, the lower plane displays the reference velocity component over the angles in black. The upper plane represents the measured velocity components in red. The blue vectors represent the transformation vectors from the measured to the reference velocity components. The  $x$ -axis displays the value of the  $v_x$  components, while the  $y$ -axis represents the  $v_y$  components. The points can also be interpreted as velocity tuple pairs.

Besides the measured points displayed in red, there are a large number of intermediate points which can be measured by the sensor. In graphical terms, this would entail the addition of numerous red and black points between the existing curves. The existence of a tangential point on the red curve that intersects the center point of the diagram ( $v_x = 0$  and  $v_y = 0$ ) would indicate that for a specific ratio of  $v_x$  and  $v_y$ , multiple translations into the ideal plane would be feasible. This ratio may also be interpreted as a perceived angle. Mathematically, given the available information, it would not be possible to distinguish between two or more different angle and velocity pairs. Given the discrete nature of the data, it is sufficient to examine the decants of the curves. If no decant of two neighboring points crosses the center points (or comes close to them), the transformation from measurement to ideal plane can be made unambiguously. In the top-down view shown in Figure 4.11b, it can be clearly seen that no such decant exists.

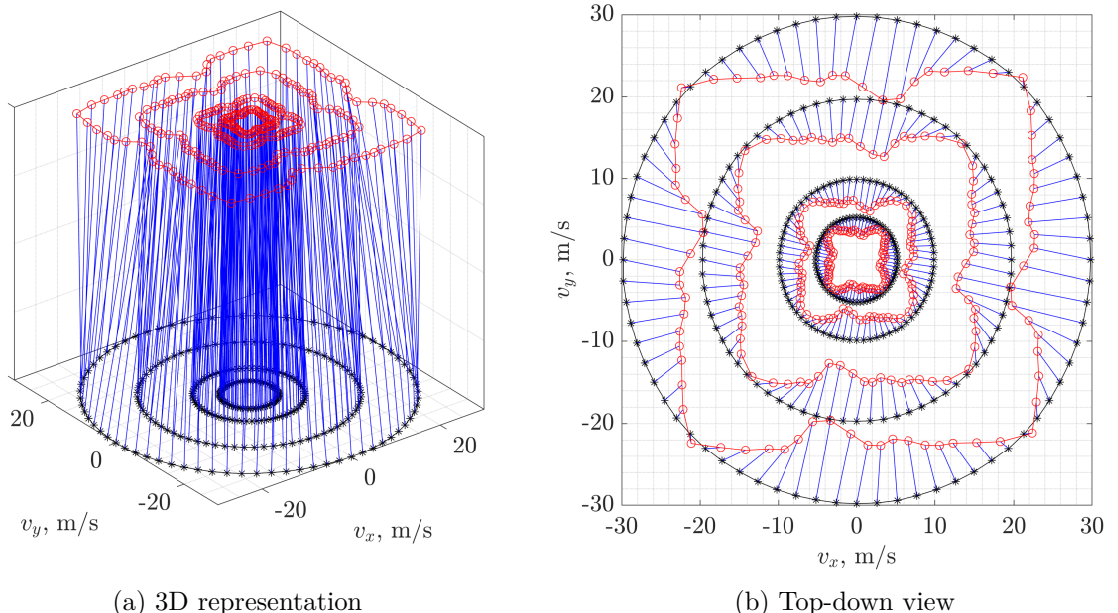


Figure 4.11: Transformation from measurement plane to reference plane

Due to the transceiver shadow effect and the resulting discrepancies (see Figure 4.10) in the ideal values, different correction methods are employed and compared on the basis of the same set of data. The data used to fit the correction method and a validation data set are presented herewith. To fit the measurements taken from  $-45^\circ$  to  $45^\circ$  scanned in  $5^\circ$  intervals at speeds of 5 m/s, 10 m/s, 20 m/s and 30 m/s, a scan was conducted. A second set of measurement points, with 100 samples of randomly placed angles at air speeds of 8 m/s, 15 m/s, 25 m/s and 35 m/s is used for validation.

### Uncorrected Velocities

In order to evaluate the subsequent enhancements of the various approaches, it is first necessary to examine the uncorrected state. For this purpose, the data is plotted in the form of a polar plot, comprising the angles of the sensor with respect to the air stream and the measured velocity magnitude. The orange star-shaped points represent the reference measurement points. The reference points are obtained using, the angle of the sensor to the air stream, and the recorded velocity either from the DANTEC anemometer or the velocity obtained by the Prandtl tube, depending on the speed regime. The blue circles represent the mean measured (and corrected) values of the sensor. The velocity magnitude is displayed on the radial-axis, while the angle is displayed on the  $\theta$ -axis. The identical configuration will be employed in subsequent comparisons. All used data is filtered with a mean filter with a window size of two samples due to the azimuth regions with high standard deviations examined in Chapter 4.4.

Figure 4.12 depicts the uncorrected data. It becomes increasingly evident that discrepancies

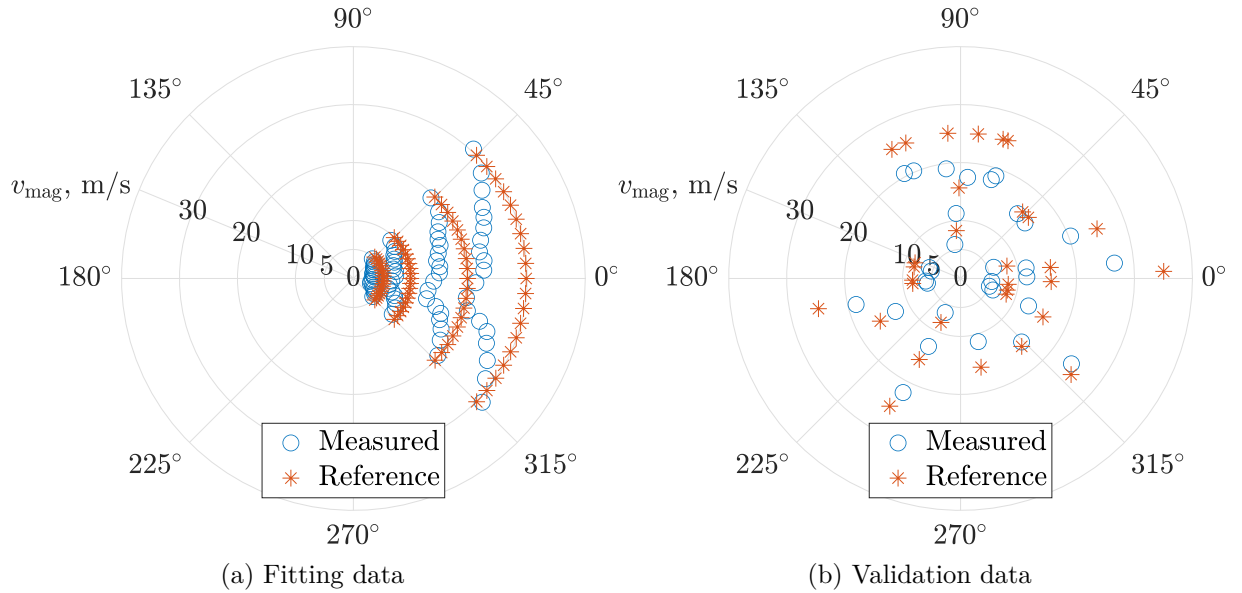


Figure 4.12: Uncorrected measured results and reference values

arise in proximity to the  $0^\circ$  mark (see Figure 4.12a). A review of Figure 4.10 elaborates that the velocity deficit is markedly greater for angles close to the  $0^\circ$  and  $90^\circ$  marks. Which coincides with the larger discrepancies near  $0^\circ$  seen in Figure 4.10. Conversely, in Figure 4.12a the velocities at  $-45^\circ$  and  $45^\circ$  appear to be in closer alignment with their ideal counterparts, which intern correlates with the lower velocity deficits seen in Figure 4.10 at  $45^\circ$ .

Over all the discrepancies are quite large and result in an nearly unusable sensor. For example the maximal velocity magnitude error is about  $10.02\text{ m/s}$  at  $30\text{ m/s}$  which results in an measurement error of  $33.4\%$  of the total reference velocity magnitude. The measurement error of the angle is  $< 5.52^\circ$ . The validation data set depicted in Figure 4.12b does not fare any better, exhibiting a significant discrepancy at all points.

Given the considerable discrepancies between the uncorrected and reference velocities, it is evident that some form of correction is necessary to obtain viable results from the sensor. The subsequent sections will examine correction methods in ascending order of complexity.

### Kaimal-Gaynor Correction

The Kaimal-Gaynor correction was implemented in accordance with Section 2.2, with a correction coefficient of  $C = 0.6$ . The corrected velocity pairs exhibit a closer resemblance to the ideal pairs. Figure 1 illustrates that the curvature of the measured velocity pairs appears to follow the curvature of the reference pairs more closely than in Figure 4.12a. A small dip (at  $-10^\circ$ ) and rise (at  $10^\circ$ ) can be observed near  $0^\circ$ . This defect is caused by the unsymmetrical nature of the velocity deficit, as illustrated in Figure 4.10. This is a limitation of the Kaimal-Gaynor correction. It assumes a symmetrical velocity deficit caused by the transceivers, which will inevitably result in a measurement error if this criterion is not met.

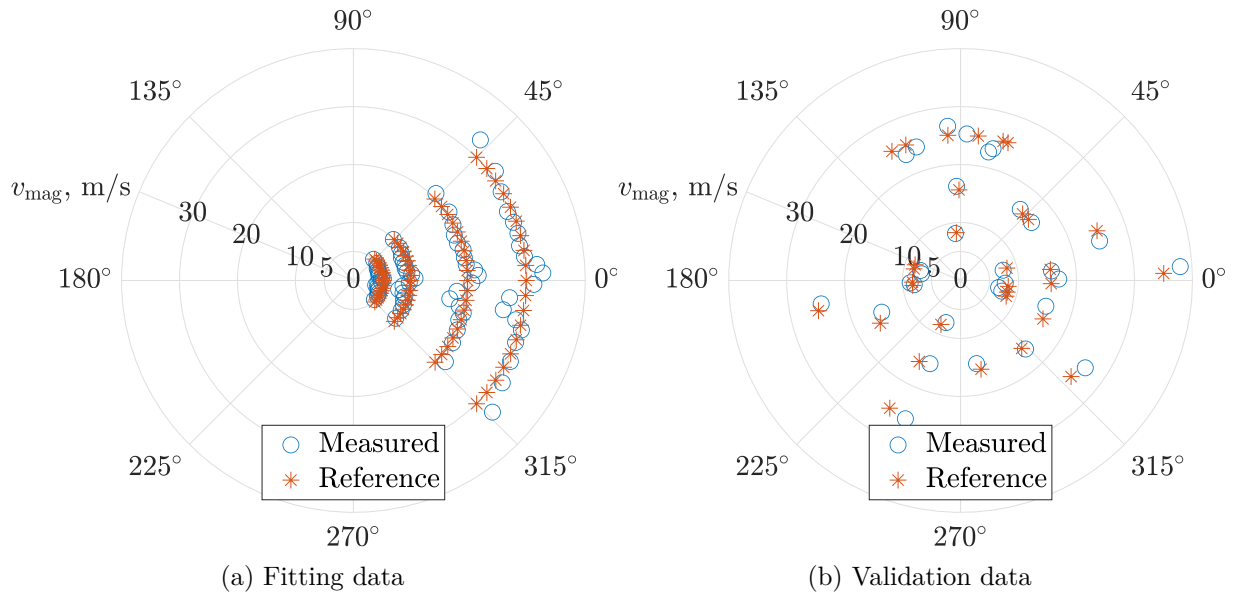


Figure 4.13: Kaimal-Gaynor corrected measurement data and reference values

The overall measurement error obtained using the fitting data is halved, the maximal velocity magnitude error is reduced to 3.38 m/s, which results in a measurement error of approximately 11.3% of the reference maximum velocity magnitude. The maximal error occurs near 0°, and is a result of the dip in velocity displayed in Figure 4.10. The error of the angle measurement rises to 9.55° which is nearly a doubling in error.

The application of the correction to the validation data (Figure 4.12b) shows a large improvement compared to the uncorrected results, the resulting maximal velocity magnitude error is 3.09 m/s. Due to the mentioned limitation of the Kaimal-Gaynor correction, a still considerable measurement error occurs around 0°.

### Map Correction

The map correction approach is based on three so called maps which hold different kinds of information. A map holds a finite amount of discrete data points which can be determined through the use of the fitting data set.

To make the creation easier the velocities and angles can be represented as vectors, where the first element (indexed which a “1”) is the lowest value and the others are in increasing order.

The maps are determined as follows:

$$(C_{\text{meas,ang,m}})_j = \frac{1}{N_{\text{vel}}} \cdot \sum_{i=1}^{N_{\text{vel}}} (\alpha_{\text{meas,m}})_{i,j} \quad (4.4)$$

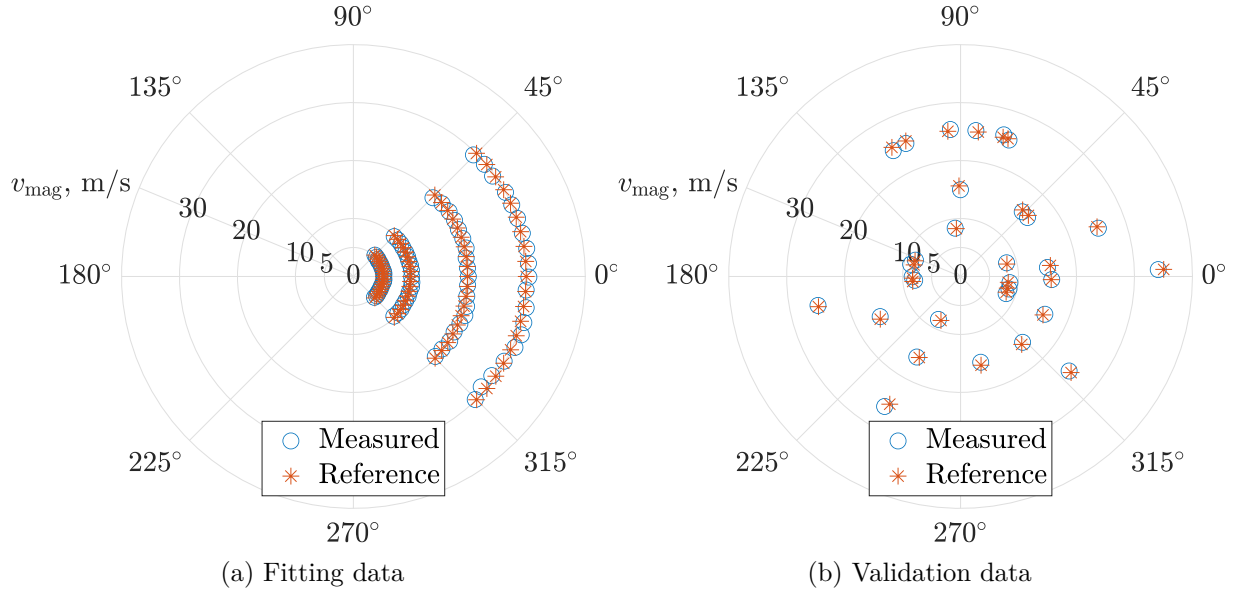


Figure 4.14: Map corrected measurement data and reference values

$$(C_{\text{meas,mag,m}})_i = \frac{1}{N_{\text{ang}}} \cdot \sum_{j=1}^{N_{\text{ang}}} (v_{\text{mag,meas,m}})_{i,j} \quad (4.5)$$

$$(C_{\text{gain,m}})_{i,j} = \frac{(v_{\text{mag,meas,m}})_{i,j}}{(v_{\text{ref}})_i} \quad (4.6)$$

where  $N_{\text{vel}}$  is the number of different reference velocities used and  $\alpha_{\text{meas,m}}$  the mean measured angle, at the speed corresponding with index  $i$  at the angle corresponding to  $j$ . The number of angles is denoted as  $N_{\text{ang}}$ . The variable  $v_{\text{ref},i}$  denotes the velocity of the corresponding reference measurement. Due to the periodic nature of the angle a first and last element is added to mitigate wrapping errors. The first element is the copy of the last regular value and vice versa. The correction of velocity and angle are done separately. To apply the correction, an interpolation between the different points in the maps takes place.

To correct the velocity  $v_{\text{mag,meas}}$ , the gain correction matrix  $C_{\text{gain,m}}$  has to be interpolated. A 2D spline interpolation scheme is used. The correction vectors  $C_{\text{meas,angle,m}}$  and  $C_{\text{meas,mag,m}}$  are used to determine  $\alpha_{\text{meas}}$  and  $v_{\text{mag,meas}}$  to the corresponding indexing for interpolation in the gain correction matrix. The resulting gain of the interpolation is denoted as  $g_{\text{interp}}$ .

$$v_{\text{mag,corr}} = v_{\text{mag,meas}} \cdot g_{\text{interp}} \quad (4.7)$$

The angle is corrected by a simple 1D interpolation of the angle correction vector  $C_{\text{meas,mag,m}}$ , the reference angle to determine as well as the measured angle  $\alpha_{\text{meas}}$ , resulting in the corrected angle  $\alpha_{\text{corr}}$ .

The correction results in visibly improved over all measurements, each blue circles overlap its red star-shaped counterpart (compare Figure 4.14). No dip or rise is visible near the  $0^\circ$  mark, the correction seems to be equally accurate over all angles and velocity.

This approach yields a velocity magnitude error smaller than 0.92 m/s for both datasets. The mean velocity magnitude error is about 0.32 m/s. Notably, the maximal empirical standard deviation rises from around 0.59 m/s from the uncorrected to 0.96 m/s after applying the correction, resulting in an increase of 62.7%.

### Matrix Correction

In this approach a matrix is used to translate the measured components  $v_x$  and  $v_y$  directly into corrected velocities  $v_{x,c}$  and  $v_{y,c}$ .

To save memory, only positive measured velocities are used to index the matrix. This is roughly equal to one quadrant of the azimuth of the sensor. If one of the measured velocities is negative, its negative sign is removed and the velocities are swapped due to the point symmetry nature of the sensor. If both velocities are negative, only the sign is removed. These steps are inverted after correction with the matrix. In the event that the measured velocity components exceed the maximum velocity described by the input vectors of the matrix, the velocity will be reduced to the aforementioned maximum velocity.

Each matrix index corresponds to a measured velocity, the intermittent distance between increments is denoted  $\delta_v$ . The corresponding uncorrected velocities are displayed as the vector along the Matrix 4.8.

$$\underbrace{\begin{bmatrix} v_x \\ 0 \\ \delta_v \\ \vdots \\ (n-2) \cdot \delta_v \\ (n-1) \cdot \delta_v \end{bmatrix}}_{v_x} \quad \overbrace{\begin{bmatrix} & & & & v_y \\ 0 & \delta_v & \dots & (n-2) \cdot \delta_v & (n-1) \cdot \delta_v \\ [v_{x,c}, v_{y,c}]_{1,1} & [v_{x,c}, v_{y,c}]_{1,2} & \dots & [v_{x,c}, v_{y,c}]_{1,n-1} & [v_{x,c}, v_{y,c}]_{1,n} \\ [v_{x,c}, v_{y,c}]_{2,1} & \ddots & & & \vdots \\ \vdots & & \ddots & & \vdots \\ [v_{x,c}, v_{y,c}]_{n-1,1} & & \ddots & & \vdots \\ [v_{x,c}, v_{y,c}]_{n,1} & \dots & \dots & \dots & [v_{x,c}, v_{y,c}]_{n,n} \end{bmatrix}}^{v_y} \quad (4.8)$$

The implementation has a matrix size of  $n = 100$  and  $\delta_v = 0.3$  resulting in a max component velocity of  $v_{x,\max} = v_{y,\max} = 29.7$  m/s. The tuples  $[v_{x,c}, v_{y,c}]$  are the corresponding corrected velocities of the combination  $[v_x, v_y]$ . These corrected values have to be determined based on the existing measurement data.

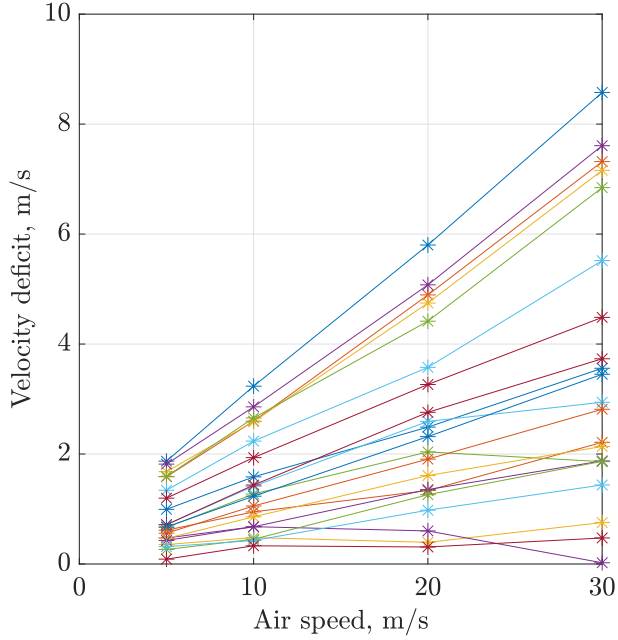


Figure 4.15: Velocity deficit across air speed

For the generation of virtual measurement points first the velocity deficit is examined (see Figure 4.15). The  $x$ -axis represents the air speed in m/s, while the  $y$ -axis depicts the velocity deficit in m/s. Each graph illustrates the velocity deficit at a specific angle of measurement. Overall, the majority of graphs exhibits an approximately linear trend, with only a few graphs (for example the lower purple graph) deviating from this trend. The total error due to the linear approximation is marginal.

The virtual measurement points are created, in order to determine the corrected values between the measured velocities and angles (“in between points”). In the initial stage, points between velocities at measurement angles are generated based on the assumption that the velocity deficit increases in a linear trend with the air velocity at a given angle (see Figure 4.16). Nevertheless, this assumption is not always accurate due to irregular behavior at specific angles and the non-linearity at some points of the trend. These virtual measurement points are the measurements the model predicts the sensor would measure at these in between air speeds.

The generated intermediate lines are depicted in blue in Figure 4.16. The black graphs represent the calculated reference velocities that the sensor should have measured under ideal circumstances. The red graphs represent the actual measured values. The left-hand side of the diagram shows the velocity measured at the  $x$ -measurement path of the sensor, while the right-hand side displays the values measured at the  $y$ -measurement path. Between the measured angles (at a given air speed) points are generated through the use of linear interpolation. For each of the generated points a virtual reference point can be created with the use of the reference speeds and the angle of the virtual measurement resulting in two tuple pairs  $[[v_x, \text{prediction}, v_y, \text{prediction}], [v_{x,c}, v_{y,c}]]_{v_{ref}, \alpha}$  these pairs can be described as a mathematical set  $D$ . These pairs can be interpreted as points in

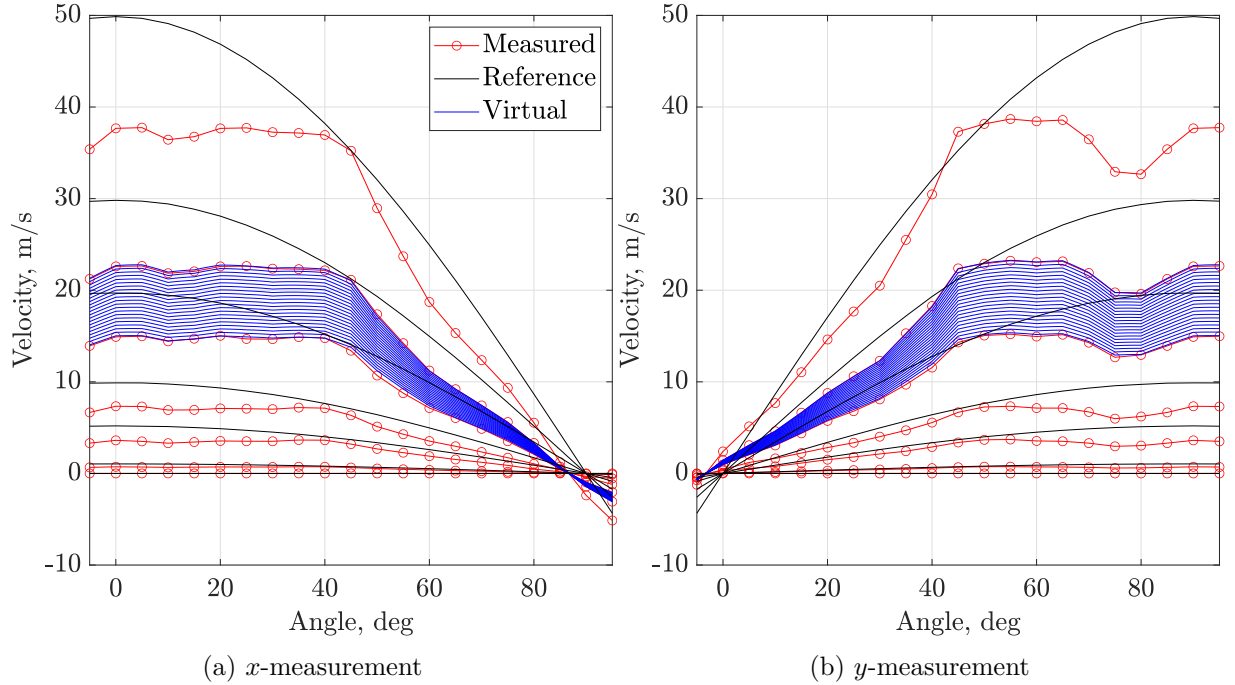


Figure 4.16: Measured and reference values across a quadrant with virtual measurements

the measured to the ideal plane, as illustrated in Figure 4.11. The matrix represents the bijective transformation between the points of the planes.

For each of the vector combinations the corresponding prediction of the set  $D$  with the lowest discrepancy is used. Following equation is used:

$$[[v_x, v_y], [v_{x, c}, v_{y, c}]] = \min \left\{ \sqrt{(v_x - v_{x, \text{prediction}})^2 + (v_y - v_{y, \text{prediction}})^2} \mid \forall d \in D \right\} \quad (4.9)$$

The correction is applied using a linear 2D interpolation between four points of matrix 4.8 the indices can be decoded from the measured velocity component with the help of the corresponding velocity vectors. The result is a fully corrected pair of velocity components.

Using this method of correction yields in good overall measurement deviations (compare Figure 4.17). No larger discrepancies are visible in the figures. The maximum velocity error is 0.43 m/s for the fitting data set and 0.86 m/s for the validation data set resulting in a measurement error of 1.4% and 2.5% respectively. The maximum angle error is 3.03° and was recorded in the validation data set.

### Comparison

In this chapter the results of aforementioned corrections will be compared. The comparison will be carried out on the validation data set due to the fitting being carried out on the fitting data set and thus resulting error would not be representative.

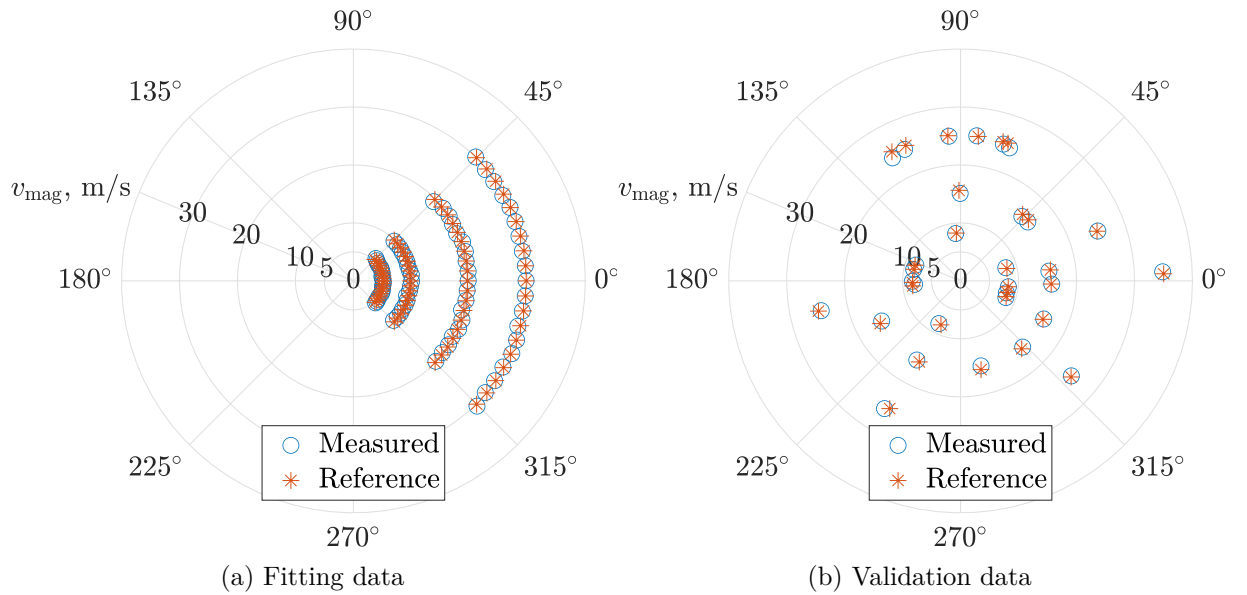


Figure 4.17: Lookup table corrected measurement data and reference values

Table 4.1: Measurement error of the corrections applied to the validation data set

| Error \ Method                               | Kaimal-Gaynor | Map  | Matrix |
|--|---------------|------|--------|
| $\Delta v_{\text{mag}, \text{m, max, m/s}}$  | 3.09          | 0.91 | 0.86   |
| $\Delta v_{\text{mag}, \text{m, mean, m/s}}$ | 0.88          | 0.31 | 0.23   |
| $\sigma_{\text{vel, mag, max, m/s}}$         | 0.56          | 1.01 | 0.79   |
| $\sigma_{\text{vel, mag, mean, m/s}}$        | 0.23          | 0.31 | 0.27   |
| $\Delta \alpha_{\text{m,max, deg}}$          | 8.21          | 3.34 | 3.03   |
| $\Delta \alpha_{\text{m,mean, deg}}$         | 3.58          | 1.27 | 1.25   |
| $\sigma_{\text{ang, max, deg}}$              | 1.88          | 2.50 | 2.51   |
| $\sigma_{\text{ang, mean, deg}}$             | 1.00          | 1.17 | 1.17   |

A summary of the error in question can be found in Table 4.1. The symbols  $\Delta v_{\text{mag}, \text{m, max}}$  and  $\Delta v_{\text{mag}, \text{m, mean}}$  represent the maximum and mean error of the mean measured and corrected data points respectively. The symbol  $\sigma$  represents the empirical standard deviation, which is expressed in an analog scheme. The resulting error in the measurement of angles is expressed in an analog manner.

It can be observed that as the complexity of the correction increases, the mean and maximal measurement error of the mean measurement value decreases. It is notable that the empirical standard deviation increases with the application of more complex correction schemes. The empirical standard deviation of the uncorrected measurement is comparable to that of the Kaimal-Gaynor correction. The increase in the empirical standard deviation is particularly pronounced at the maximum value of the empirical standard deviation.

This lead to the conclusion that certain areas exist where the correction is badly conditioned and an error amplification takes place. The gradient fields displayed in Figure 4.18, represents the absolute gradient of the corrected velocity on the  $z$ -axis and the uncorrected velocities are displayed on the  $x$ - and  $y$ -axis. A high gradient means that a small change in measured velocity results in a large change in the corrected velocity component. This means that measurement errors get over proportionally amplified in areas with a high gradient. For small ratios of  $\frac{v_x}{v_y}$  both gradients are comparably high resulting in a high error amplification in both corrected components. Which intern leads to a high deviation in measured angle and magnitude. These small ratios coincide with small angles. So the maximum error amplification is to be expected at small angles, due to the mapping of the correction to all for quadrant these area are to be expected to be symmetrical and occurring at every  $90^\circ$  interval.

These areas of comparably high gradients coincide with the dip noticeable in Figure 4.11 and are due to the low information density at these points.

Some of the resulting errors in the correction can be attributed to the underlying assumption that the measurement error is point symmetric across the sensor azimuth. This error could be caused by a not sufficiently accurate calibration of zero offset and linearity, or an overall limitation of the assumption. But due to the overall low maximum mean velocity deviation, it can be assumed that the assumption of symmetry in the measured velocity is met sufficient.

Both the map and matrix correction yield satisfactory results. However, it is debatable whether the higher memory usage and complexity of the matrix correction are worthwhile in light of the small but consistent gains in accuracy. As a consequence of the increased complexity, it may be more challenging to identify and rectify any errors that may arise. It is possible that errors may occur if the correction is applied to a different sensor of the same design due to variants in components and slight deviations in geometric shape. The quantity of measurement data required for the reconstruction of both approaches is identical. Both corrections result in overall low computation time and complexity. However, the matrix approach can be considered simpler and faster in its application.

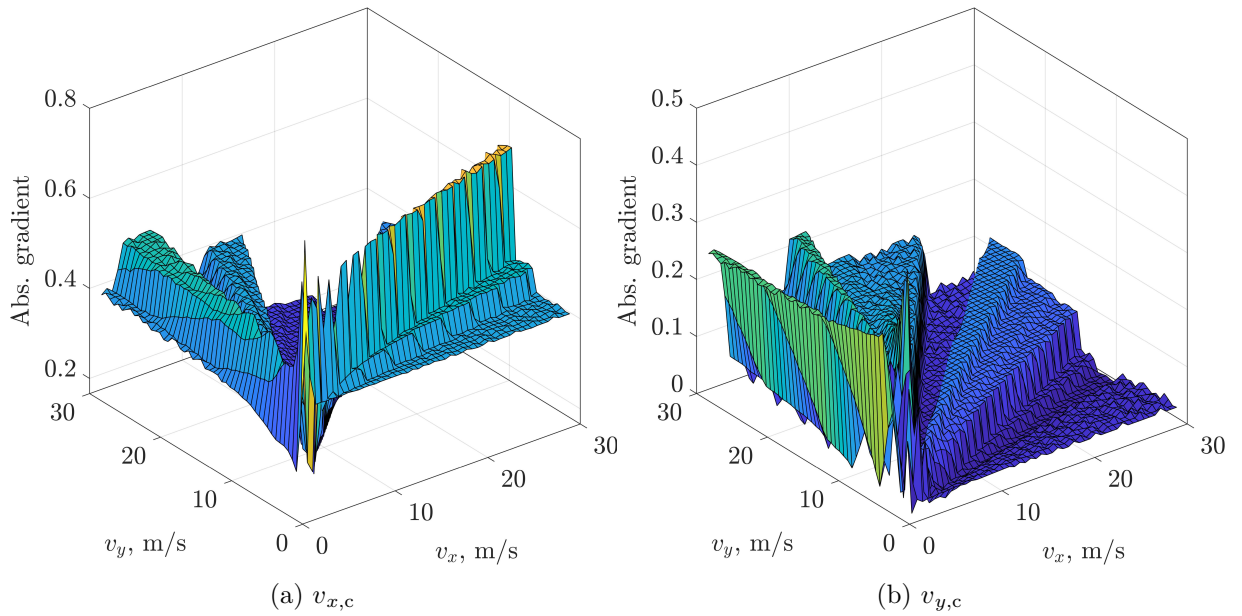


Figure 4.18: Absolute gradient of Matrix 4.8

Figure 4.19 displays the normalized root mean square (RMS) on the  $y$ -axis, the RMS is normalized with the reference speed. The  $x$ -axis displays the reference speed. As a bases of the Figure 4.19, the validation data set was used. Due to the limit amount of measurement point, 10 measurements per reference speed, the error might be not representative.

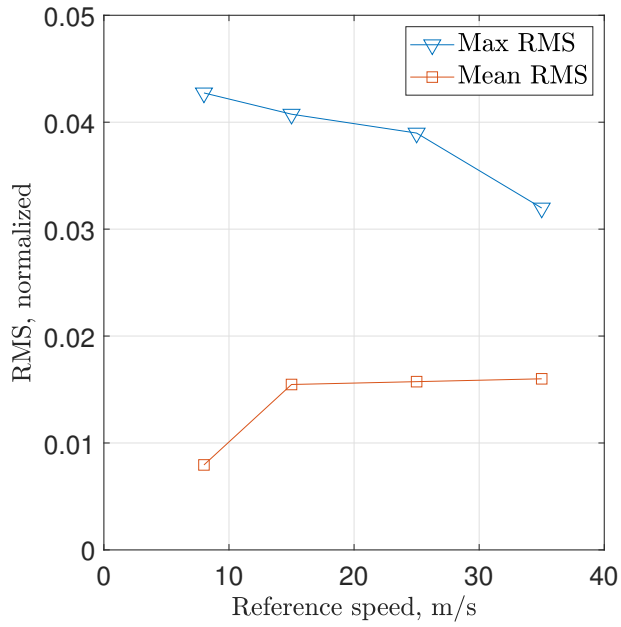


Figure 4.19: RMS normalized, across Reference speed

The trend of the maximum RMS (in orange) is declining with higher reference speeds, while the mean RMS (in blue) is approximately constant for reference speeds above 15 m/s. The maximum

normalized mean RMS is 1.6% at 35 m/s while the maximum normalized RMS is 4.3% at 8 m/s. The large difference between the mean and maximum normalized RMS is to be expected due to the large difference in the standard deviation over the angles.

Comparing the error to a commercially available Thies 2D ultrasonic anemometer (4.3875.xx.xxx), which has a stated accuracy  $\pm 2\%$  RMS for air speeds over 5 m/s at a comparable measurement rate of 100 Hz [12]. The build sensor has a comparable mean RMS but maximum RMS exceeds the state error by about two times. This is partly due to the larger build size of the Thies anemometer.

The build does not achieve the desired measurement accuracy at 10 m/s with the maximum velocity error of  $\pm 0.35$  m/s at 8 m/s and  $\pm 0.63$  m/s at 15 m/s both exceeding the desired error of  $\pm 0.1$  m/s.

## 5 Conclusion and Outlook

A miniaturized ultrasonic anemometer has been designed, build and tested. The goal of this project is to create an ultrasonic anemometer that can be integrated into the existing measuring infrastructure of DLR and used to measure the outwash of hovering aircraft. The sensor has been tested in a wind tunnel for the purpose of further evaluation. The resulting measurements have been employed to calibrate the sensor and characterize the measurement error. The measurement error can be classified into two categories: statistical and absolute. The statistical error was found to be highly dependent on the angle of the sensor relative to the inflow. This high degree of dependency is attributed to the vortex shedding of the upstream transceiver, which gives rise to a kind of transceiver vortex effect. The vortices result in an elongation and shrinking of the measurement path, which cause a change in perceived delay, the change in distribution has been demonstrated. The magnitude of the effect can be attributed to the low  $L/d$  ratio, which results in a significant portion of the measurement path being subject to the disturbance. The effectiveness of mean and median filters in reducing the statistical error of the sensor has been evaluated.

The absolute measurement error can be attributed to the transceiver shadow effect, which is the result of a decline in mean velocity along the measurement path caused by the blockage of the flow by the transceiver. Given the irregular behavior of the measurements at a fixed reference speed, as a function of the angle of the sensor with respect to the inflow, an evaluation of the potential for ambiguity in the correction of the absolute error has been conducted, and it has been determined that such ambiguity is indeed unambiguously possible. Three distinct correction methodologies have been subjected to evaluation and comparison. Two of the examined correction schemes yielded satisfactory results in terms of error reduction. However, the overall error remained above the desired measurement error threshold. This was attributed to the low  $L/d$  ratio, which emerged as a crucial design parameter for ultrasonic anemometers, even at reduced scale. Despite the elevated overall error, the sensor's performance remained satisfactory.

To limit the transceiver shadow effect and the impact of vortex shedding of the transceiver, a sensor with a larger  $L/d$  ratio can be build, this step highly recommended. While the angle depended velocity deficit of the transceiver shadow effect is rectifiable the statistical error caused by vortices is not. To increase  $L/d$  ratio either the Transceiver diameter can be decreased or the measurement path elongated.

The over all accuracy of the measurement can be increased by using higher frequency transceivers, it has to be noted that sound absorption of air increases with rising frequencies and ADC

sampling rate has to be increased rustling in higher complexity. The increased accuracy, assuming a comparable sub-period accuracy of the matched filter, is due to the decreased absolute error caused by the decreased timer per period. High frequency transceivers are often available in smaller form factors.

For higher measurement frequencies a faster microcontroller can be used as well as shorter phase shift keys decreasing the send and receive times.

A more drastically approach is to rethink the measurement principle and us a single point sound source and place microphones around aforementioned sound source allowing for a measurement of all directions at once. This would allow for the use of much small and cost effective MEMS (Micro-Electro-Mechanical Systems) microphones, due to lack need to transmit and receive. Another benefit is the higher measuring frequencies possibly ranging into the kilohertz range. The point source could be realized by the use of an electric arc for example.

The field of sonic velocimetry still has many new and exciting possibilities for further development and optimization, making it a promising field of velocimetry.

## List of Symbols

### Acronyms

| Acronym | Description   |
|---------|---|
| IO      | Input and output  |
| PCB     | Printed circuited board   |
| AC      | Alternating current   |
| DC      | Direct current  |
| ADC     | Analog to digital converter   |
| DAC     | Digital to analog converter   |
| GPIO    | General purpose in- and output  |
| DMA     | Direct memory access  |
| UART    | Universal aAsynchronous receiver / transmitter                                  |
| CRC32   | Cyclic redundancy check 32-bit  |
| SRAM    | Serial random access memory   |
| IC      | Integrated circuit  |
| DLR     | Deutsches Zentrum für Luft- und Raumfahrt<br>( <i>German aerospace center</i> ) |
| SPI     | Serial peripheral interface   |
| ToF     | Time of Flight  |
| PPR     | Primary peak ratio  |
| RMS     | Root mean square  |
| MEMS    | Micro-electro-mechanical systems  |

## Symbol

| Symbol       | Description                                     | SI unit                |
|--------------|---|------------------------|
| $l, L$       | Length of the measurement path                  | m                      |
| $v$          | Flow velocity                                   | m/s                    |
| $t$          | Delay   | s                      |
| $a$          | Speed of sound                                  | m/s                    |
| $A$          | Matrix of speed of sound candidates             | m/s                    |
| $C, c$       | Correction factor                               | -                      |
| $d$          | Diameter of the transceiver                     | m                      |
| $t_0$        | Delay of the match signal                       | s                      |
| $n$          | Natural number                                  | -                      |
| $N$          | Total amount                                    | -                      |
| $g_{interp}$ | Interpolated gain                               | -                      |
| $D$          | Mathematical set of tuple pairs                 | -                      |
| $f, g$       | Discrete signals or function                    | -                      |
| $T$          | Matrix of delays                                | s                      |
| $s$          | Score of a candidate                            | -                      |
| $S$          | Score matrix                                    | -                      |
| $x$          | In or resulting of a measurement in x direction |                        |
| $y$          | In or resulting of a measurement in y direction |                        |
| $T_0$        | Temperature while recording the match           | K                      |
| $R_L$        | Ideal gas constant of Air                       | $\frac{J}{kg \cdot K}$ |
| $\sigma$     | Empirical standard deviation                    | -                      |
| $\alpha$     | Angle of the sensor to the air stream           | deg                    |
| $\theta$     | Angle of the air stream to the measurement path | deg                    |
| $\delta_v$   | Velocity increment                              | m/s                    |
| $\kappa$     | Isotropic exponent                              | -                      |

## Index

| Indices    | Description                         |
|------------|-------------------------------------|
| m          | Mean                                |
| corr       | Corrected                           |
| c          | Corrected                           |
| ortho      | Orthogonal                          |
| meas       | Measured                            |
| rel        | Relative                            |
| ref        | Reference                           |
| mag        | Magnitude                           |
| max        | Maximum                             |
| min        | Minimum                             |
| 0          | Initial value                       |
| off        | Offset of Speed                     |
| +          | Resulting of positive signed values |
| -          | Resulting of negative signed values |
| ang        | Angle                               |
| vel        | Velocity                            |
| prediction | Value of a prediction               |
| AB         | From transceiver A to B             |
| BA         | From transceiver B to A             |
| CD         | From transceiver C to D             |
| DC         | From transceiver D to C             |
| air        | Speed of the air along the path     |
| reduced    | Reduced values of a matrix          |
| pp         | Peak to peak                        |

## Literature

- [1] Y. Tanabe, H. Sugawara, S. Sunada, K. Yonezawa, and H. Tokutake, “Quadrotor drone hovering in ground effect,” *Journal of Robotics and Mechatronics*, vol. 33, no. 2, pp. 339–347, 2021. DOI: 10.20965/jrm.2021.p0339.
- [2] A. A. Flem, M. Ghirardelli, S. T. Kral, E. Cheynet, T. O. Kristensen, and J. Reuder, “Experimental characterization of propeller-induced flow (pif), below a multi-rotor uav,” *Atmosphere*, 2024. DOI: 10.3390/atmos15030242.
- [3] A. J. Wadcock, L. A. Ewing, E. Solis, M. Potsdam, and G. Rajagopalan, “Rotorcraft downwash flow field study to understand the aerodynamics of helicopter brownout,” in *AHS Southwest Region Technical Specialist’s Meeting "Technologies for Next Generation of Vertical Life Aircraft"*, 2008.
- [4] J. N. Braukmann, C. Schwarz, C. C. Wolf, E. Buron, S. Koch, G. Buske, and A. D. Gardner, “Bos and hot-film analysis of a ch-53g helicopter wake in ground effect,” in *Vertical Flight Society 80th Annual Forum*, 2024. DOI: 10.4050/F-0080-2024-1060.
- [5] Calypso Instruments. “Ultra-low-power ultrasonic wind meter ulp standard.” (), [Online]. Available: <https://calypsoinstruments.com/shop/product/ultra-low-power-ultrasonic-wind-meter-ulp-standard-6?category=2#attr=76,71,65> (visited on 07/08/2024).
- [6] H. Lau. “Ultraschall windmesser / ultraschall anemometer.” (), [Online]. Available: <https://www.dl1glh.de/ultraschall-anemometer.html> (visited on 06/03/2024).
- [7] P. Steven W. Smith. “The scientist and engineer’s guide to digital signal processing.” (), [Online]. Available: <http://www.dspsguide.com/ch17/3.html> (visited on 06/04/2024).
- [8] del Valle, M. Perez, Castelan, J. A. Urbano, Matsumoto, Yasuhiro, and R. C. Mateos, “Low cost ultrasonic anemometer,” in *4th International Conference on Electrical and Electronics Engineering*, 2007, pp. 213–216. DOI: 10.1109/ICEEE.2007.4345008.
- [9] J. C. Kaimal and J. E. Gaynor, “The boulder atmospheric observatory,” *Journal of Applied Meteorology and Climatology*, 1983. DOI: 10.1175/1520-0450(1983)022<0863:TBAO>2.0.CO;2.
- [10] T. Shimizu, M. Suzuki, and A. Shimizu, “Examination of a correction procedure for the flow attenuation in orthogonal sonic anemometers,” *Boundary-Layer Meteorology* 93, 1999. DOI: 10.1023/A:1002053313130.

- [11] C. Wolff. “Intrapulse modulation.” (2016), [Online]. Available: <https://www.radartutorial.eu/druck/Book7.pdf> (visited on 07/15/2024).
- [12] Adolf Thies GmbH Co. KG. “Ultraschall anemometer 2d compact.” (), [Online]. Available: <https://www.thiesclima.com/de/Produkte/Wind-Messtechnik-Ultraschall-Anemometer/> (visited on 07/08/2024).